William S. Rone
Department of Mechanical Engineering,
Virginia Tech,
Randolph Hall, Room 8,
460 Old Turner Street (0710),
Blacksburg, VA 24061
e-mail: wsrone@vt.edu

Wael Saab
Department of Mechanical Engineering,
Virginia Tech,
Randolph Hall, Room 8,
460 Old Turner Street (0710),
Blacksburg, VA 24061
e-mail: waelsaab@vt.edu

Pinhas Ben-Tzvi[1]
Department of Mechanical Engineering,
Virginia Tech,
Goodwin Hall, Room 465,
635 Prices Fork Road (0238),
Blacksburg, VA 24061
e-mail: bentzvi@vt.edu

Design, Modeling, and Integration of a Flexible Universal Spatial Robotic Tail

This paper presents the novel design of a bioinspired robot capable of generating spatial loading relative to its base. By looking to nature at how animals utilize their tails, a bioinspired structure is developed that utilizes a redundant serial chain of rigid links to mimic the continuous deformation of a biological tail. Individual links are connected by universal joints to enable a spatial robot workspace capable of generating spatial loading comprised of pitch, yaw, and roll direction contributions. Two sets of three cables are used to create two actuated segments along the robot. A dynamic model of the robot is derived using prescribed cable displacement trajectories as inputs to determine the resulting joint angle trajectories and cable tensions. Sensors are integrated on-board the robot to calculate joint angles and joint velocities in real-time for use in feedback control. The loading capabilities of the robot are analyzed, and an experimental prototype is integrated and demonstrated. [DOI: 10.1115/1.4039500]

1 Introduction

The dominant approach for legged locomotion is to propel, maneuver, and stabilize the robot using its legs during locomotion. In bipeds, for example, this stems from the primary focus on mimicking humanoid locomotion. However, looking to legged animals, tails are commonly observed to perform one or more functions that assist in locomotion ranging from propulsion [1,2] to maneuvering [3,4] to stabilization [5,6]. In addition, these tail structures can also provide manipulation capabilities as well [7].

Although prior research has looked into incorporating robotic tails into legged systems, in order to justify the inclusion of a tail structure on-board a mobile robot, it must be able to perform a variety of tasks across several of these categories. The Universal Spatial Robotic Tail (USRT) presented in this paper is a serpentine robot with a spatial workspace capable of generating controlled spatial loading (relative to the yaw, pitch, and roll principle axes).

This paper focuses on the design, modeling, and integration of the USRT, one of the three potential robotic tail structures under investigation by the authors [8–10]. This paper builds on the work presented in Ref. [8] by implementing the USRT prototype and utilizing this prototype along with the USRT's dynamic model to generate loading in the yaw, pitch, and roll directions. Figure 1 illustrates a preliminary design concept for a bipedal legged robot constructed of RMLeg modules [11] with the USRT attached. Future work will analyze the scaling of the USRT required to utilize the robot's spatial loading to effectively stabilize and maneuver a legged platform. Furthermore, although tail-based applications are the primary focus of the research associated with the USRT, broader work is also planned for this structure, including aquatic propulsion using octopuslike tentacles and fishlike tails, energy harvesting using a flexible structure, aerospace robots using flexible structures to conserve momentum in maneuvering satellites, and snakelike ground propulsion.

This paper is organized into the following sections: Section 2 presents previous work associated with inertial adjustment mechanisms, robotic tails, and hyperredundant robots, along with the requirements that motivated the robot's design. Section 3 presents the USRT's mechanical design. Section 4 presents the kinematic and dynamic models of the USRT. Section 5 analyzes the USRT's workspace and the loading generated by yaw, pitch, and roll motions of the USRT. Section 6 details the methodologies for joint angle and joint velocity state estimation using sensors embedded along the USRT. Section 7 discusses the experimental prototype of the USRT and compares measured loading results to those generated by the dynamic model in simulation. Section 8 concludes the work and discusses ongoing research.

2 Background and Design Motivation

This section reviews inertial adjustment mechanisms used in a broad range of engineering applications and motivates the design of the USRT. Inertial adjustment mechanisms are discussed to identify potential candidates for integration onto mobile robotic systems (Sec. 2.1), which leads to a comparative design review of existing robotic tails (Sec. 2.2). Then, the field of articulated, hyperredundant robotics (Sec. 2.3) is reviewed to identify the design criteria that have inspired the USRT (Sec. 2.4).

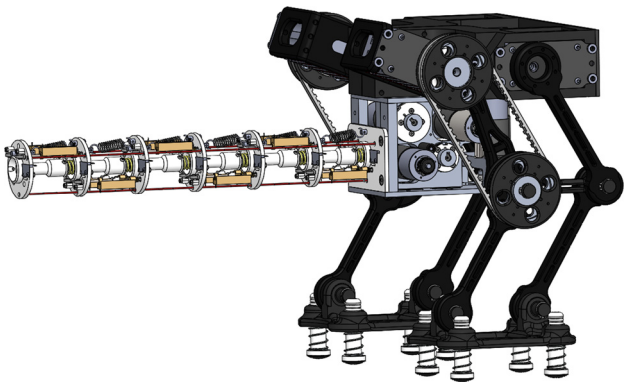

Fig. 1 Design concept for bipedal robot with USRT

[1]Corresponding author.

Contributed by the Mechanisms and Robotics Committee of ASME for publication in the Journal of Mechanisms and Robotics. Manuscript received October 24, 2017; final manuscript received February 21, 2018; published online April 5, 2018. Assoc. Editor: Leila Notash.

2.1 Inertial Adjustment Mechanisms. Inertial adjustment mechanisms are defined by their ability to adjust the center-of-mass (COM) location of a system and/or generate loading at/about their attachment point. These mechanisms may be categorized based on their principle of operation: (i) substrate interaction mechanisms (such as thrusters, jets, and fans) propel liquid or gas to produce force, (ii) translational mechanisms (also called reaction masses) displace a mass to generate force and adjust COM location, (iii) symmetric rotational mechanisms (such as reaction wheels) rotate a mass with the COM intersecting the axis of rotation to generate moments, and (iv) asymmetric rotation mechanisms (such as pendulums) rotate a mass with COM offset from the axis of rotation to generate forces and moments and adjust the COM location.

Although category (i) mechanisms have effectively demonstrated inertial adjustment capabilities, additional components required for operation such as propellers, compressors, and fuel are not typically needed by a mobile robot, making practical implementation challenging. Similarly, the effectiveness of category (ii) mechanisms would be limited to the reaction mass's range of motion, and the mechanism would require a large footprint for proper operation.

Category (iii) reaction wheels are compact in size and have been more extensively studied in the literature [12] compared to category (iv) pendulums as inertial adjustment mechanisms. However, a pendulum can be designed with significantly larger moment of inertia than a reaction wheel for a given mass due to the moment of inertia's quadratic dependency on the distance between the joint axis and COM. However, its implementation requires a larger workspace and may be limited by interference with the mobile robot or ground. Comparative analysis of the angular impulse between a robotic tail, in the form of a rigid-body pendulum, and reaction wheels has shown that a tail can provide significantly higher loading in short time frames, making it more appropriate for use when space is available for a high moment of inertia mechanism, while reaction wheels can provide moment profiles over longer timespans based on the controlled acceleration and deceleration of a reaction wheel as it continuously rotates [13]. Thus, a category (iv) mechanism is best suited to act as a robotic tail.

2.2 Robotic Tail Designs. Robotic tails in the literature draw inspiration from animals such as fish [14,15], cheetahs [16,17], and lizards [18]. However, unlike their biological inspiration, terrestrial robotic tail designs focus primarily on single degree-of-freedom (DOF) pendulumlike structures operating in the yaw [19–21], pitch [17,22], or roll [23] directions. Two degrees-of-freedom pendulums have also been demonstrated in the pitch–yaw [24–26] and pitch–roll [16] directions. Functionally, these tails have been used to aid propulsion [17,19,27], maneuvering [18,20,21,23,24], and stabilization [16,25,26].

Recent research has shown the favorable impact that the use of articulated higher-DOF robotic tail structures can have on the loading profiles transmitted to the mobile robot [11,28]. Furthermore, motions associated with different mode shapes of multisegment tails capable of forming multiple curvatures along their lengths enable greater flexibility for COM positioning and dynamic loading [29]. However, practical implementation of this articulation requires more complex mechanical designs and actuators for controlled motion. Therefore, the authors aim to continue efforts in analyzing the benefits of an articulated tail design realized using a hyperredundant mechanism.

2.3 Potential Design Candidates: Hyperredundant Robots. In nature, a wide variety of biological structures (such as tails, tentacles, snakes' bodies, and elephants' trunks) have morphologies which can be considered as hyperredundant, which are characterized by having numerous redundant DOFs. Continuum and serpentine robots are two types of hyperredundant robots that are analogous in shape and articulation to these biological structures [30]. Continuum robots are defined by their theoretically infinite DOFs and are capable of bending along their length. Serpentine robots are composed of a serial chain of numerous, similar (often identical) rigid links capable of forming discretized curvatures.

Designs for continuum robots can be classified by their forms of actuation. Intrinsically actuated designs are constructed of smart materials that generate motion in addition to providing the robot's structure, such as pneumatic artificial muscles [31], shape memory alloys [32], and bellows [33]. Extrinsically actuated designs are composed of an elastic core that provides structural support and distributes the actuation applied by cables or rods along the structure [34–36]. Extrinsic designs provide the benefit of using common forms of rotary or linear actuation that can be mounted at the robot's base and transmitted along the robot, facilitating miniaturization and reducing the minimum robot mass.

Traditional serpentine robots are designed by connecting rigid bodies/modules with individually actuated revolute joints in parallel (for planar motion) or skewed (for spatial motion) orientations [37]. Variations of this methodology utilize parallel mechanisms [38], angular bevel joints [39], and universal joints actuated with ball screw-driven belt trains [40]. Conventional means of modeling and sensing using rotary encoders can be applied to such designs; however, individual joint actuation increases the robot's mass, cross section, and actuator torque requirements. To address these challenges, underactuating the serpentine mechanism has been studied, utilizing cable-driven actuation with angular deflection regulated by an elastic core [41] or rolling contact joints [42]. The merits of cable-driven serpentine robots have been demonstrated in robotic exoskeleton planar finger designs that couple joint motion via friction pulleys [43], higher order rolling pairs [44], and spring-loaded joints [45].

2.4 Design Requirements. Before discussing the USRT specifically, the motivating factors which led to this design (and the others under consideration by the authors) are presented. The most fundamental requirement of the robot is that it be multifunctional. In order to justify the inclusion of such a structure onboard a mobile robot, it must be capable of spatial motion to allow it to generate generalized spatial loading in the yaw, pitch, and/or roll directions.

Furthermore, the robot should be capable of high-speed dynamic motions during operation. Many of the hyperredundant structures presented in Sec. 2.3 are designed to operate in quasi-static equilibrium, in which the dynamic effects of the robot can be neglected. These robots cannot demonstrate the high-speed motions that may be necessary in some applications to generate dynamic loading in the system.

The system must also be designed for effective cantilevered operation. A key shortcoming of continuum robots is the high stiffness required in the structure to resist excessive sag when cantilevered. Existing macroscale continuum robots use pneumatics or coil springs to form their structures, but pneumatics do not permit controlled highly dynamic motion, and coil spring structures have only been demonstrated in vertical hanging orientations [46]. As a result, the robot will be implemented as a serpentine structure.

Looking to existing serpentine structures, a key decision is whether to individually actuate joints or to utilize an underactuated approach. To increase the number of links along the robot and localize actuation at the base, this research utilizes an underactuated design. This paper studies the use of elastic loading between subsegments to distribute the actuation loading within a segment, instead of kinematic coupling that prescribes relative motion between links [9,10].

Finally, the robot should be capable of forming multiple curvatures along its length, with its segments capable of being actuated at least quasi-independently of one another and actuation localized at the base. Single-segment robots are more limited in their

COM workspace than multisegment robots, and greater flexibility in positioning (quasi-static) and moving (dynamic) the COM provides greater functionality. Localizing actuation at the base will allow for greater control over the robot dynamics by reducing the need to incorporate bulky actuators along the structure.

3 System Design

This section details the design of the USRT, including the robot's structure (Sec. 3.1), elastic elements (Sec. 3.2), actuation (Sec. 3.3), and sensing (Sec. 3.4).

3.1 Robot Structure. The USRT, shown in Fig. 2, is composed of a serial chain of six links connected by universal joints that permit relative pitch and yaw. The six links are organized into two quasi-independently actuated segments 1 and 2 (further discussed in Sec. 3.3).

Figures 3 and 4 show subsegment i between disks $i-1$ and i. In addition to the universal joint between these links, two springs are mounted (extension and compression, Sec. 3.2), along with actuation cabling (Sec. 3.3), two distance sensors (Sec. 3.4), and a joint angle limit.

The joint angle limit prevents the angular displacement of the universal joint from exceeding a fixed maximum angle. To implement the joint limit, a pair of axisymmetric beveled surfaces are incorporated into the designs of disk $i-1$ and the base of central link i. The beveled surfaces are parallel and in contact when the joint angle limit is reached, and the axisymmetric design allows the surface to "roll" along the mated beveled surfaces at the maximum deflection as the joint's pitch and yaw angles are varied. This provides a uniform maximum workspace for each joint when planning the robot's motion and prevents the need for the displacement sensors to stop joint motion at their limits.

Although the universal joints only permit relative pitch and yaw between links, a rolling motion can be created by multiple subsegments acting together, as shown in Fig. 5. In this illustration, the pitch and yaw angles are varied sinusoidally to roll the USRT COM around the mounting plate centerline.

3.2 Elasticity. As shown in Fig. 4, two sources of elastic loading are incorporated into each subsegment: (1) a compression spring surrounding the universal joint that resists bending equally in all directions as the universal joint deflects and (2) an extension spring mounted between adjacent links to help compensate for gravitational loading.

The compression spring provides a compact means of distributing actuation loading within an actuated segment. These springs provide axisymmetric mechanical coupling between links to prevent the cable actuation from only causing bending in a single joint (the extension spring only acts in the pitch direction). The compression spring is housed within the central link, and the portion exposed between adjacent links contributes to the bending resistance.

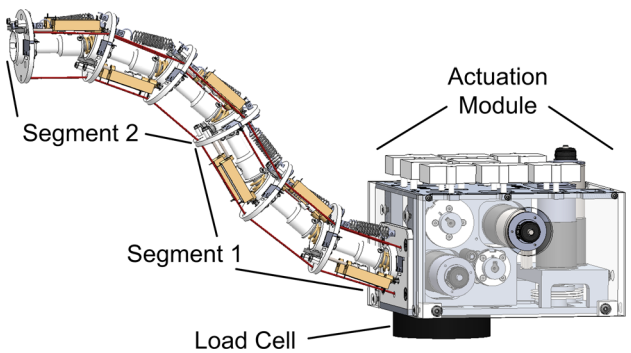

Fig. 2 Universal spatial robotic tail

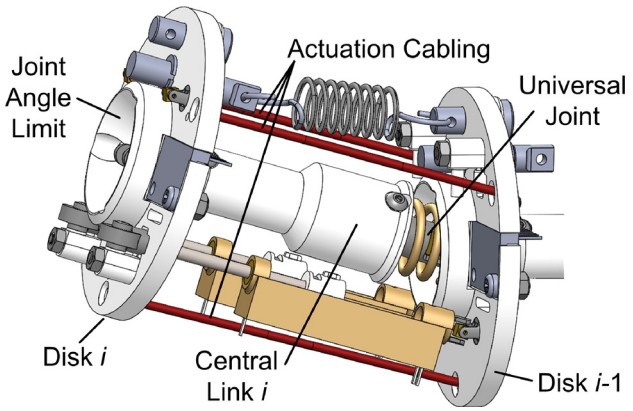

Fig. 3 USRT subsegment: structure and actuation

The extension spring modifies the joint's elasticity in the pitch direction to help offset the effect of gravity. Because of the differences in gravitational moments at joints along the robot (i.e., the gravitational moment near the base is significantly higher than the gravitational moment near the tip), the elastic loading required from this spring in each joint varies. This variation in elastic loading can be achieved by varying the springs' stiffnesses, unloaded lengths, and/or anchor-point distances. Spring stiffness and unloaded length are functions of the spring chosen for inclusion in the design; for a fixed unloaded length, higher stiffnesses correlate to higher forces, and for a fixed stiffness, shorter unloaded lengths generate higher forces for a fixed distance between anchor points. As shown in Fig. 4, the USRT design incorporates an adjustable anchor to allow for variation of the distance between anchor points. This adjustable anchor is a passive means of adjusting the extension spring loading; it is not actuated and cannot be changed during the robot's motion. The fixed anchor in Fig. 4 is designed such that the spring anchor point is an equal distance from the disk surface as the central universal joint. This minimizes the effect of the extension spring on yaw-direction loading. In addition, there is sufficient clearance in the extension spring anchor holes to accommodate the springs' motion without generating undesired friction.

3.3 Actuation. An actuated segment is created by ending/tying-off sets of three actuation cables at a specific disk. The first actuated segment is from the robot's base to the first disk to which cables are tied off, and subsequent segments are from the previous segment's terminal link to the next link at which cables are tied off. Actuation is applied by three cables routed through holes at a fixed radius with 120 deg between holes around the disk center.

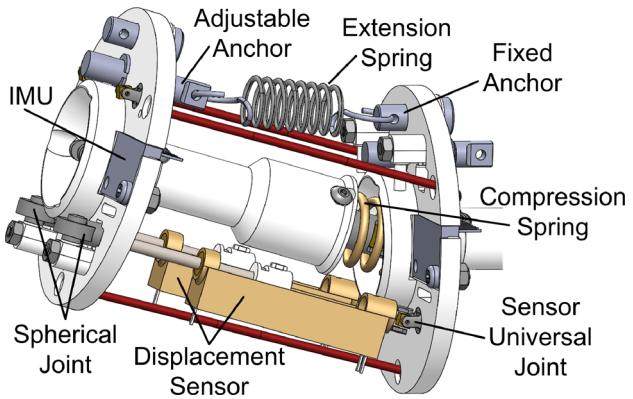

Fig. 4 USRT subsegment: elasticity and sensing

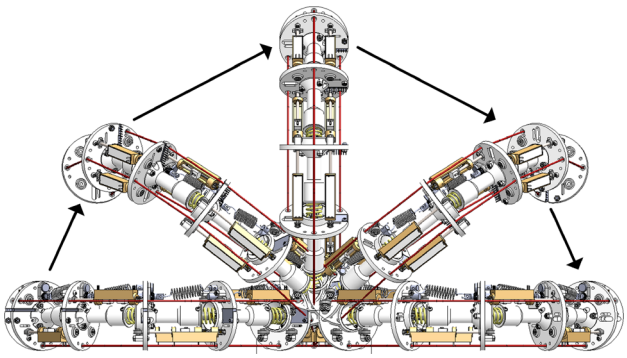

Fig. 5 Front view of a USRT rolling motion through −180 deg with the robot bent 180 deg, shown in 45 deg increments

Cables terminating in different segments are corouted through the same holes to simplify control. For example, in a two-segment structure, to account for the change in cable path lengths in segment 1 for segment 2 cabling, the prescribed segment 1 cable displacements can be added to the desired segment 2 cable displacements.

During operation, in each segment, two cables will be "active" (i.e., tensioned) and one cable will be "passive." The active cables will constrain the motion of the segment and dictate its shape. The passive cable will follow the segment trajectory established by the other two cables. It is important that the passive cable not over-slack because the subset of two active cables may change during the robot's motion.

3.4 Sensing. Sensors integrated along the robot allow for estimation of the joint angles and velocities of each universal joint. Two displacement sensors (Fig. 4) are mounted between the disks separated by each joint to measure the distances between pairs of fixed points on each disk. These distances can be used to analytically calculate the pitch and yaw joint angles of the universal joint, providing a mechanism for sensing the real-time robot configuration.

An inertial measurement unit (IMU, Fig. 4) that includes a gyroscope is also mounted to each link. Utilizing the body-fixed angular velocity measurements from the gyroscope, along with the estimates of the relative pitch and yaw of adjacent links from the displacement sensors, the universal joint pitch and yaw velocities may also be estimated.

4 Universal Spatial Robotic Tail Mechanics

This section presents the kinematic (Sec. 4.1) and dynamic (Sec. 4.2) models of the USRT.

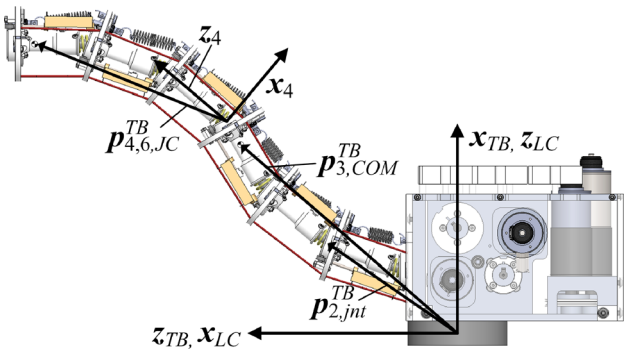

Fig. 6 USRT frame definitions and joint/link COM vectors

4.1 Universal Spatial Robotic Tail Kinematics. The USRT is modeled as a cable-driven serial robot defined by six universal joints (or 12 revolute joints) and four cable displacement inputs. The state variables are six joint pitch angles φ_i, six joint yaw angles θ_i, and four cable tensions T_j, where cables $j=\{A,B\}$ terminate in segment 1 and cables $j=\{C,D\}$ terminate in segment 2. The pair $\{A,B\}$ will be a nonrepeating subset of $\{1,2,3\}$, and the pair $\{C,D\}$ will be a nonrepeating subset of $\{4,5,6\}$.

As an initial step, the orientation and position kinematics are defined. Frames for the USRT base (TB) and a USRT link (link 4) are shown in Fig. 6. The link i orientations with respect to both link $i-1$ ($\boldsymbol{R}_i^{i-1}$) and the USRT base frame ($\boldsymbol{R}_i^{\mathrm{TB}}$) are defined in Eq. (1), where $\mathbf{I}_3$ is the three × three identity matrix, $\boldsymbol{R}_Y(\varphi)$ is the rotation matrix for a y-axis rotation by angle φ, and $\boldsymbol{R}_X(\theta)$ is the rotation matrix for an x-axis rotation by angle θ. Throughout this paper, superscripts denote the frame in which a vector is defined (except T, which denotes transpose).

$$\boldsymbol{R}_i^{i-1}=\boldsymbol{R}_Y(\varphi_i)\boldsymbol{R}_X(\theta_i),\quad \boldsymbol{R}_i^{\mathrm{TB}}=\begin{cases}\mathbf{I}_3 & i=0\\ \boldsymbol{R}_{i-1}^{\mathrm{TB}}\boldsymbol{R}_i^{i-1} & i>0\end{cases} \tag{1}$$

Using these orientations, the position vectors from the USRT base frame origin to joint i ($\boldsymbol{p}_{i,\mathrm{jnt}}^{\mathrm{TB}}$) and the link i center-of-mass ($\boldsymbol{p}_{i,\mathrm{COM}}^{\mathrm{TB}}$), shown in Fig. 6, may be calculated using Eqs. (2) and (3), where $\boldsymbol{p}_{01,\mathrm{jnt}}^{\mathrm{TB}}$ is the position vector from the TB frame to joint 1, L_{JJ} is the distance between adjacent universal joints, $\boldsymbol{z}_i^j$ is the frame i z-axis defined in frame j, $\boldsymbol{p}_{0,\mathrm{JC}}^{\mathrm{TB}}$ is the position vector from the TB frame origin to the link 0 COM, and L_{JC} is the distance from joint i to the link i COM (Fig. 7)

$$\boldsymbol{p}_{i,\mathrm{jnt}}^{\mathrm{TB}}=\begin{cases}\boldsymbol{p}_{01,\mathrm{jnt}}^{\mathrm{TB}} & i=1\\ \boldsymbol{p}_{i-1,\mathrm{jnt}}^{\mathrm{TB}}+L_{\mathrm{JJ}}\boldsymbol{R}_i^{\mathrm{TB}}\boldsymbol{z}_i^i & i>1\end{cases} \tag{2}$$

$$\boldsymbol{p}_{i,\mathrm{COM}}^{\mathrm{TB}}=\begin{cases}\boldsymbol{p}_{0,\mathrm{JC}}^{\mathrm{TB}} & i=0\\ \boldsymbol{p}_{i,\mathrm{jnt}}^{\mathrm{TB}}+L_{\mathrm{JC}}\boldsymbol{R}_i^{\mathrm{TB}}\boldsymbol{z}_i^i & i>0\end{cases} \tag{3}$$

The link i angular velocity may be defined relative to link $i-1$ ($\boldsymbol{\omega}_{(i-1)i}^{i-1}$) and the USRT base frame ($\boldsymbol{\omega}_i^{\mathrm{TB}}$), as defined in the below equation, where $\dot{\varphi}$ denotes the first-time derivative of φ, and $\boldsymbol{x}_i^j$ and $\boldsymbol{y}_i^j$ are the frame i x- and y-vectors, respectively, defined with respect to frame j

$$\boldsymbol{\omega}_{(i-1)i}^{i-1}=\dot{\varphi}_i\boldsymbol{y}_{i-1}^{i-1}+\dot{\theta}_i\boldsymbol{x}_i^{i-1},\quad \boldsymbol{\omega}_i^{\mathrm{TB}}=\begin{cases}\mathbf{0} & i=0\\ \boldsymbol{\omega}_{i-1}^{\mathrm{TB}}+\boldsymbol{R}_{i-1}^{\mathrm{TB}}\boldsymbol{\omega}_{(i-1)i}^{i-1} & i>0\end{cases} \tag{4}$$

An additional set of kinematic variables are also needed to characterize the bending angle and plane of each universal joint for calculating the compression spring loading. The angle β_i (>0) between the frame $i-1$ z-axis and the frame i z-axis is defined in the below equation, along with the unit vector $\boldsymbol{\lambda}_i^{i-1}$ along the common normal between these two axes (assuming they are not coincident), where $\tilde{\boldsymbol{a}}\boldsymbol{b}$ denotes the cross product $\boldsymbol{a}\times\boldsymbol{b}$

$$\beta_i=\mathrm{a\cos}\left(\left(\boldsymbol{z}_{i-1}^{i-1}\right)^T\boldsymbol{R}_i^{i-1}\boldsymbol{z}_i^i\right),\quad \boldsymbol{\lambda}_i^{i-1}=\tilde{\boldsymbol{z}}_{i-1}^{i-1}\boldsymbol{R}_i^{i-1}\boldsymbol{z}_i^i/\sin\beta_i \tag{5}$$

The product $\dot{\beta}_i \boldsymbol{\lambda}_i^{i-1}$ for the universal joint damping may be formulated in terms of $\boldsymbol{\omega}_{(i-1)i}^{i-1}$ using the below equation, which isolates the x- and y-components of the relative angular velocity

$$\dot{\beta}_i \boldsymbol{\lambda}_i^{i-1} = \left(\boldsymbol{x}_{i-1}^{i-1}\left(\boldsymbol{x}_{i-1}^{i-1}\right)^T + \boldsymbol{y}_{i-1}^{i-1}\left(\boldsymbol{y}_{i-1}^{i-1}\right)^T\right)\boldsymbol{\omega}_{(i-1)i}^{i-1} \tag{6}$$

To aid in calculating the gravitational and inertial moments, position vectors from joint i to the link j COM are defined as $\boldsymbol{p}_{i,j,\mathrm{JC}}$ in the below equation and shown in Fig. 6

$$\boldsymbol{p}_{i,j,\mathrm{JC}}^{\mathrm{TB}} = \boldsymbol{p}_{j,\mathrm{COM}}^{\mathrm{TB}} - \boldsymbol{p}_{i,\mathrm{jnt}}^{\mathrm{TB}} \tag{7}$$

For extension spring i, Eq. (8) defines $\boldsymbol{p}_{i,\mathrm{JE}}^{i}$ as the position from joint i to the spring i tip anchor and $\boldsymbol{p}_{i,\mathrm{ex}}^{i-1}$ as the position from the spring i base to tip, shown in Fig. 7, where L_{JD} is the distance from joint i to the link i disk center, $\boldsymbol{p}_{i,\mathrm{ex},T}^{i}$ is the link i position from disk center to extension spring tip, $\boldsymbol{p}_{\mathrm{ex},B}^{i-1}$ is the link $i-1$ position from disk center to extension spring base, and L_{DJ} is the distance from the link $i-1$ disk center to joint i

$$\boldsymbol{p}_{i,\mathrm{JE}}^{i} = L_{\mathrm{JD}}\boldsymbol{z}_i^i + \boldsymbol{p}_{i,\mathrm{ex},T}^{i}, \quad \boldsymbol{p}_{i,\mathrm{ex}}^{i-1} = -\boldsymbol{p}_{\mathrm{ex},B}^{i-1} + L_{\mathrm{DJ}}\boldsymbol{z}_{i-1}^{i-1} + \boldsymbol{R}_i^{i-1}\boldsymbol{p}_{i,\mathrm{JE}}^{i} \tag{8}$$

For the actuation cabling, Eq. (9) defines $\boldsymbol{p}_{i,j,\mathrm{JH}}^{i}$ as the position from joint i to the disk i cable routing hole j and $\boldsymbol{p}_{i,j,\mathrm{cbl}}^{i-1}$ as the cable j position from disk $i-1$ to disk i, shown in Fig. 7, where $\boldsymbol{p}_{j,\mathrm{hl}}^{i}$ is the position from a disk's center to its cable j routing hole. The displacement $\delta_{j,k}$ of cable j terminating in segment k due to the robot's configuration is defined by Eq. (10)

$$\boldsymbol{p}_{i,j,\mathrm{JH}}^{i} = L_{\mathrm{JD}}\boldsymbol{z}_i^i + \boldsymbol{p}_{j,\mathrm{hl}}^{i}, \quad \boldsymbol{p}_{i,j,\mathrm{cbl}}^{i-1} = -\boldsymbol{p}_{j,\mathrm{hl}}^{i-1} + L_{\mathrm{DJ}}\boldsymbol{z}_{i-1}^{i-1} + \boldsymbol{R}_i^{i-1}\boldsymbol{p}_{i,j,\mathrm{JH}}^{i} \tag{9}$$

$$\delta_{j,k} = \sum_{i=1}^{3k}\left(\|\boldsymbol{p}_{i,j,\mathrm{cbl}}^{i-1}\| - L_{\mathrm{JJ}}\right) \tag{10}$$

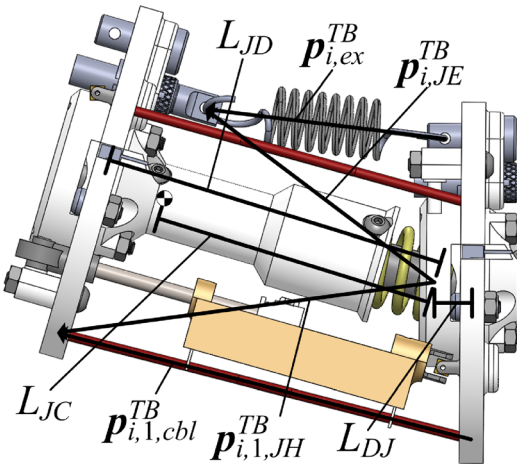

Fig. 7 USRT subsegment kinematics definitions

4.2 Universal Spatial Robotic Tail Dynamics. Four types of loading are considered in the dynamics model: inertia, gravity, coupling, and actuation. To compute the robot's dynamic equilibrium, the net moment due to these sources of loading is found at each joint, and the components of this net moment aligning with the pitch and yaw joint axes are prescribed as zero (a revolute joint cannot support a moment about its joint axis).

A joint's gravitational and inertial moments are due to the gravitational and inertial loading acting on the COMs of links "downstream" of the joint. Equation (11) defines the link j gravitational force $\boldsymbol{F}_{j,\mathrm{grv},L}^{\mathrm{TB}}$, inertial force $\boldsymbol{F}_{j,\mathrm{inr},L}^{\mathrm{TB}}$, and inertial moment $\boldsymbol{M}_{j,\mathrm{inr},L}^{\mathrm{TB}}$, where m_j is the link j mass, g is the gravitational acceleration, $\boldsymbol{I}_j^{\mathrm{TB}}$ is the link j inertia defined in the TB frame, and $\boldsymbol{I}_j^j$ is the constant link j body-frame inertia. The joint i gravitational $\boldsymbol{M}_{i,\mathrm{grv}}$ and inertial $\boldsymbol{M}_{i,\mathrm{inr}}$ moments are due to the loading acting on links j through 6, as defined in Eq. (12)

$$\begin{aligned}
\boldsymbol{F}_{j,\mathrm{grv},L}^{\mathrm{TB}} &= -m_j g\boldsymbol{x}_{\mathrm{TB}}^{\mathrm{TB}}, & \boldsymbol{I}_j^{\mathrm{TB}} &= \boldsymbol{R}_j^{\mathrm{TB}}\boldsymbol{I}_j^j\left(\boldsymbol{R}_j^{\mathrm{TB}}\right)^T,\\
\boldsymbol{F}_{j,\mathrm{inr},L}^{\mathrm{TB}} &= m_j\ddot{\boldsymbol{p}}_{i,\mathrm{COM}}^{\mathrm{TB}}, & \boldsymbol{M}_{j,\mathrm{inr},L}^{\mathrm{TB}} &= \boldsymbol{I}_j^{\mathrm{TB}}\dot{\boldsymbol{\omega}}_j^{\mathrm{TB}} + \tilde{\boldsymbol{\omega}}_j^{\mathrm{TB}}\boldsymbol{I}_j^{\mathrm{TB}}\boldsymbol{\omega}_j^{\mathrm{TB}}
\end{aligned} \tag{11}$$

$$\begin{aligned}
\boldsymbol{M}_{i,\mathrm{grv}}^{\mathrm{TB}} &= \sum_{j=i}^{6}\left(\tilde{\boldsymbol{p}}_{i,j,\mathrm{JC}}^{\mathrm{TB}}\boldsymbol{F}_{j,\mathrm{grv},L}^{\mathrm{TB}}\right)\\
\boldsymbol{M}_{i,\mathrm{inr}}^{\mathrm{TB}} &= \sum_{j=i}^{6}\left(\boldsymbol{M}_{j,\mathrm{inr},L}^{\mathrm{TB}} + \tilde{\boldsymbol{p}}_{i,j,\mathrm{JC}}^{\mathrm{TB}}\boldsymbol{F}_{j,\mathrm{inr},L}^{\mathrm{TB}}\right)
\end{aligned} \tag{12}$$

The joint i coupling moment $\boldsymbol{M}_{i,\mathrm{cpl}}^{i-1}$, defined in Eq. (13), is due to the loading acting between links $i-1$ and i. Four sources of loading are included in Eq. (13): the extension spring, the compression spring, the joint damping, and the joint angle limit

$$\boldsymbol{M}_{i,\mathrm{cpl}}^{i-1} = \boldsymbol{M}_{i,\mathrm{ex}}^{i-1} + \boldsymbol{M}_{i,\mathrm{cmp}}^{i-1} + \boldsymbol{M}_{i,\mathrm{dmp}}^{i-1} + \boldsymbol{M}_{i,\mathrm{lim}}^{i-1} \tag{13}$$

For the joint i extension spring, $\boldsymbol{M}_{i,\mathrm{ex}}^{i-1}$ is defined in the below equation, where $k_{i,\mathrm{ex}}$ is the spring i stiffness, $L_{i,\mathrm{ex}}$ is the spring i unloaded length, and $F_{i,\mathrm{ex}}$ is the spring i pretension, where $\hat{\boldsymbol{p}}$ denotes the unit vector of $\boldsymbol{p}$

$$\boldsymbol{M}_{i,\mathrm{ex}}^{i-1} = \tilde{\boldsymbol{p}}_{i,\mathrm{JE}}^{i-1}\boldsymbol{F}_{i,\mathrm{ex}}^{i-1}, \quad \boldsymbol{F}_{i,\mathrm{ex}}^{i-1} = -\left(k_{i,\mathrm{ex}}\left(\|\boldsymbol{p}_{i,\mathrm{ex}}^{i-1}\| - L_{i,\mathrm{ex}}\right) + F_{i,\mathrm{ex}}\right)\hat{\boldsymbol{p}}_{i,\mathrm{ex}}^{i-1} \tag{14}$$

The joint i compression spring generates a moment $\boldsymbol{M}_{i,\mathrm{cmp}}^{i-1}$ that resists the joint's net deflection β_i, as defined in Eq. (15), where $k_{i,\mathrm{cp}}$ is the spring i bending stiffness [47]. Equation (15) also defines the joint damping $\boldsymbol{M}_{i,\mathrm{dmp}}^{i-1}$, which approximates energy loss during subsegment motion due to dissipative effects (e.g., friction), where $c_{i,\mathrm{dmp}}$ is the joint i effective damping

$$\boldsymbol{M}_{i,\mathrm{cmp}}^{i-1} = -k_{i,\mathrm{cp}}\beta_i\boldsymbol{\lambda}_i^{i-1}, \quad \boldsymbol{M}_{i,\mathrm{dmp}}^{i-1} = -c_{i,\mathrm{dmp}}\dot{\beta}_i\boldsymbol{\lambda}_i^{i-1} \tag{15}$$

The joint angle limit (Sec. 3.1) that prevents β_i from exceeding an angle β_{lim} generates a moment $\boldsymbol{M}_{i,\mathrm{lim}}^{i-1}$ with respect to the joint when the calculated β_i exceeds β_{lim}. The joint angle limit is modeled as a nonlinear spring damper, with zero loading when $\beta_i \leq \beta_{\mathrm{lim}}$, and continuously increasing loading if $\beta_i > \beta_{\mathrm{lim}}$, as defined in the below equation, where $k_{i,\mathrm{lim}}$ is the joint i limit's additional stiffness and $c_{i,\mathrm{lim}}(\beta_i - \beta_{\mathrm{lim}})$ is the joint i limit's additional damping

$$\boldsymbol{M}_{i,\text{lim}}^{i-1} = \begin{cases} \mathbf{0} & \beta_i \le \beta_{\text{lim}} \\ \begin{pmatrix} -k_{i,\text{lim}}(\beta_i - \beta_{\text{lim}}) \\ -c_{i,\text{lim}}(\beta_i - \beta_{\text{lim}})(\dot{\beta}_i - \dot{\beta}_{\text{lim}}) \end{pmatrix} \lambda_i^{i-1} & \beta_i > \beta_{\text{lim}} \end{cases} \tag{16}$$

The joints' actuation loading is due to the cables passing through a specific subsegment (six for segment 1 or joints 1–3 and three for segment 2 or joints 4–6). Each cable is defined by a tension T_j prescribed at the base (this tension may be zero), with coefficients $\mu_{i,j}$ scaling that tension along the robot. If $\mu_{i,j} = 0$, this implies cable j is not present in that subsegment; if $0 < \mu_{i,j} < 1$, this implies cable j's subsegment i tension is lessened by friction; if $\mu_{i,j} = 1$, the cable routes without friction. The resulting joint i actuation moment $\boldsymbol{M}_{i,\text{act}}^{i-1}$ is defined in the below equation:

$$\boldsymbol{M}_{i,\text{act}}^{i-1} = \sum_{j=1}^{6} \tilde{\boldsymbol{p}}_{i,j,\text{JH}}^{i-1} \boldsymbol{F}_{i,j,\text{cbl}}^{i-1}, \quad \boldsymbol{F}_{i,j,\text{cbl}}^{i-1} = -\mu_{i,j} T_j \hat{\boldsymbol{p}}_{i,j,\text{cbl}}^{i-1} \tag{17}$$

The coefficients $\mu_{i,j}$ are defined in two stages: First, the $\mu_{i,j}$ for all subsegments a given cable does not pass through are set to zero. For the two-segment, six cable USRT shown in Fig. 2, this condition is defined in Eq. (18) for the coefficients of cables 1–3 through subsegments 4–6

$$\mu_{i,j} = 0, \quad (i,j) = (\{4,5,6\},\{1,2,3\}) \tag{18}$$

Second, a belt-friction model [48] is assumed at each cable routing hole, and the cumulative friction losses in subsegment tensions are propagated along the length of the robot. For the belt-friction model, this is a geometric scaling, defined in Eq. (19), where μ_s is the belt coefficient of friction and $\psi_{i,j}$ is the cable j contact angle at disk i

$$\mu_{i,j} = \begin{cases} 1 & i = 0 \\ \mu_{i-1,j} e^{-\mu_s \psi_{i,j}} & i > 0 \end{cases}, \psi_{i,j} = \cos^{-1}\left(\left(\hat{\boldsymbol{p}}_{i,j,\text{cbl}}^{i-1} \right)^T \hat{\boldsymbol{p}}_{i+1,j,\text{cbl}}^{i-1} \right) \tag{19}$$

The joint i net moment $\boldsymbol{M}_{i,\text{jnt}}^{i-1}$ is defined in Eq. (20), and twelve (six pairs) joint moment constraints may be calculated using Eq. (21). Four additional constraints enforce that four of the robot's cable displacements follow the desired cable displacement trajectories $\delta_{\text{des},j,k}$ in Eq. (22), where j will be two of {1,2,3} for $k = 1$ and $k = 2$. If the second derivative of Eq. (22) is taken, the 16 equations may be organized according to Eq. (23), where $\boldsymbol{q}$ is a vector of the pitch and yaw joint angles and $\boldsymbol{T}$ is a vector of nonzero cable tensions. The matrix $\boldsymbol{A}$ in Eq. (23) is nonsingular for $0 \le \beta_i < 90$ deg, which encompasses the USRT workspace under consideration. This allows for the vector of joint angle accelerations $\ddot{\boldsymbol{q}}$ to be solved for using Eq. (23) and integrated

$$\boldsymbol{M}_{i,\text{jnt}}^{i-1} = \left(\boldsymbol{R}_{i-1}^{\text{TB}} \right)^T \left(\boldsymbol{M}_{i,\text{inr}}^{\text{TB}} - \boldsymbol{M}_{i,\text{grv}}^{\text{TB}} \right) - \boldsymbol{M}_{i,\text{cpl}}^{i-1} - \boldsymbol{M}_{i,\text{act}}^{i-1} \tag{20}$$

$$\left(\boldsymbol{y}_{i-1}^{i-1} \right)^T \boldsymbol{M}_{i,\text{jnt}}^{i-1} = 0, \quad \left(\boldsymbol{R}_i^{i-1} \boldsymbol{x}_i^i \right)^T \boldsymbol{M}_{i,\text{jnt}}^{i-1} = 0, \quad i \in \{1,\ldots,6\} \tag{21}$$

$$\delta_{\text{des},j,k} - \delta_{j,k} = 0 \quad j \in \{\{1,2\},\{2,3\},\{1,3\}\}, \; k \in \{1,2\} \tag{22}$$

$$\boldsymbol{A} \begin{bmatrix} \ddot{\boldsymbol{q}} \\ \boldsymbol{T} \end{bmatrix} = \boldsymbol{b} \iff \begin{bmatrix} \boldsymbol{A}_{11} & \boldsymbol{A}_{12} \\ \boldsymbol{A}_{21} & 0 \end{bmatrix} \begin{bmatrix} \ddot{\boldsymbol{q}} \\ \boldsymbol{T} \end{bmatrix} = \begin{bmatrix} \boldsymbol{b}_1 \\ \boldsymbol{b}_2 \end{bmatrix} \tag{23}$$

5 Workspace and Loading Analysis

This section analyzes the workspace of the USRT (Sec. 5.1) and the loading generated by the USRT due to its positioning (gravitational loading) and dynamic motion (inertial loading). A method of calculating the USRT's loading is presented in Sec. 5.2, and case studies for various USRT motions are described in Sec. 5.3.

The geometric, mass, and elastic properties used in these simulations have been extracted from a prototype of the USRT, described in Sec. 7, and its associated CAD model. Tables 1 and 2 define the USRT's properties, along with Eqs. (24) and (25). The moments of inertia of links 1–6 are sufficiently small that they may be neglected, and friction is assumed to be negligible along the length of the USRT

$$\boldsymbol{I}_0^0 = \begin{bmatrix} 0.036 & 0 & -0.001 \\ 0 & 0.032 & 0 \\ -0.001 & 0 & 0.024 \end{bmatrix} \text{kg m}^2, \quad \boldsymbol{I}_{\{1,\ldots,6\}}^{\{1,\ldots,6\}} = \mathbf{0} \tag{24}$$

$$\boldsymbol{p}_{j,\text{hl}}^i = r_{\text{hl}} \begin{bmatrix} \cos\varsigma_j & \sin\varsigma_j & 0 \end{bmatrix}^T, \quad \varsigma_j = 180^\circ + 120^\circ (j-1) \tag{25}$$

Table 1 USRT properties

Var.	Value	Var.	Value
L_{JJ}	80 mm	$\boldsymbol{p}_{01,\text{jnt}}^{\text{TB}}$	[62.85; 0; 53.5] mm
L_{JD}	74 mm	$\boldsymbol{p}_{0,\text{JC}}^{\text{TB}}$	[84.64; 0; −56.13] mm
L_{JC}	46.6 mm	$\boldsymbol{p}_{\text{ex},B}^i$	[30.5; 0; 6] mm
L_{DJ}	6 mm	$k_{i,\text{cp}}$	2.82 N·m/rad
m_0	6507 g	$c_{i,\text{dmp}}$	0.1 N m s/rad
$m_{\{1-6\}}$	85 g	β_{lim}	35 deg
r_{hl}	32.5 mm	$k_{i,\text{lim}}$	100 N·m/rad
μ_s	0	$c_{i,\text{lim}}$	0.1 N m s/rad^2

Table 2 USRT subsegment-specific properties

Jnt.	$k_{i,\text{ex}}$ (N/m)	$L_{i,\text{ex}}$ (mm)	$F_{i,\text{ex}}$ (N)	$\boldsymbol{p}_{i,\text{ex},T}^i$ (mm)
1	1460.6	38.354	3.47	[20.8; 0; −14.26]
2	1460.6	38.354	3.47	[20.8; 0; −16.18]
3	684.7	36.830	4.27	[20.8; 0; −13.45]
4	455.3	36.830	2.98	[20.8; 0; −13.39]
5	122.6	37.592	1.02	[20.8; 0; −15.38]
6	122.6	37.592	1.02	[20.8; 0; −15.57]

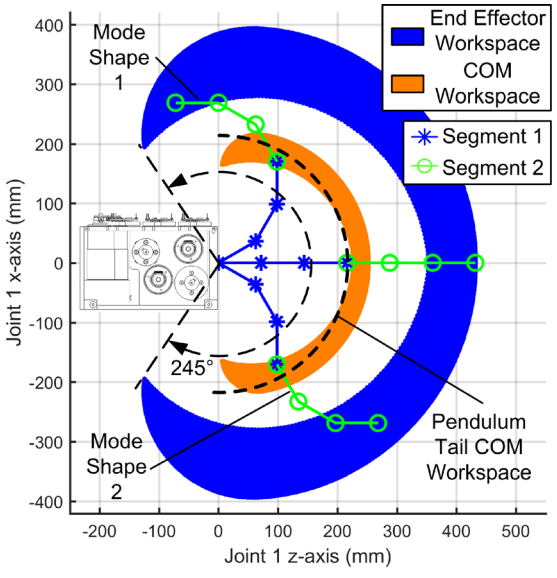

Fig. 8 Workspaces and mode shapes of a two-segment, six-link USRT

5.1 Universal Spatial Robotic Tail Workspace. The USRT is an articulated structure that can form spatial, multicurvature configurations that provide enhanced performance with a larger workspace compared to the pendulumlike robotic tails previously presented in the literature. For the USRT, the end-effector workspace is the locus of points that the terminal link (link 6) can reach, which depends on the link geometry and maximum universal joint deflection angle, and the COM workspace is the locus of points the robot's COM can reach, which depends on the link geometry, maximum universal joint deflection angle, and the robot's mass distribution. Using the USRT's geometric and mass properties defined in Table 1, Fig. 8 illustrates a cross section of the USRT's end-effector and COM workspaces taken in the $x_1 - z_1$ plane, with the coordinate frame's origin taken at joint 1. The spatial volumetric workspaces can be obtained by revolving these areas about the z_1-axis.

Since the robot is composed of two active segments, it can produce two distinct mode shapes. Mode shape 1 is illustrated as a C-curve where the segments bend in the same direction, and mode shape 2 is illustrated as an S-curve where the segments bend in opposite directions. Between these two mode shapes, intermediate mode shapes can be achieved in which the bending planes of the two segments have an angular offset. Based on the uniform mass distribution currently under consideration, the end-effector and COM workspaces span 245 deg and 180 deg, respectively.

For the single-mass pendulumlike robotic tails in the literature, both the end-effector and COM workspaces are equivalent since the tail COM is located at its end-effector (i.e., the tip of the pendulum). In the planar cross section in Fig. 8, the pendulum robotic tail workspace is a circular arc; if this pendulum was 2DOF with a universal joint, the spatial workspace would be a spherical shell. In comparison, the USRT produces volumetric COM and end-effector workspaces which provide a wider range of potential trajectories for driving the robot, and by extension, loading the legged robot [29].

The shape, scaling, and placement of the COM workspace may be adjusted by adding additional mass to the robot and/or redistributing it. Of particular interest is the ability to add mass to link 6, such that the COM workspace expands and shifts toward the end-effector workspace. Devising the optimal length, total mass, and mass distribution of the USRT is a key element of future work in tail-based task planning and control of legged robots.

5.2 Universal Spatial Robotic Tail Loading Calculation. In this analysis, it will be assumed that the USRT's base frame is coincident with the center of the load cell mounted to the USRT shown in Fig. 2 to aid in the comparison of experimental results in Sec. 7. This load cell records the force and moment acting between the USRT and its mounting; this loading is analogous to the loading the USRT would apply to a stationary mobile robot.

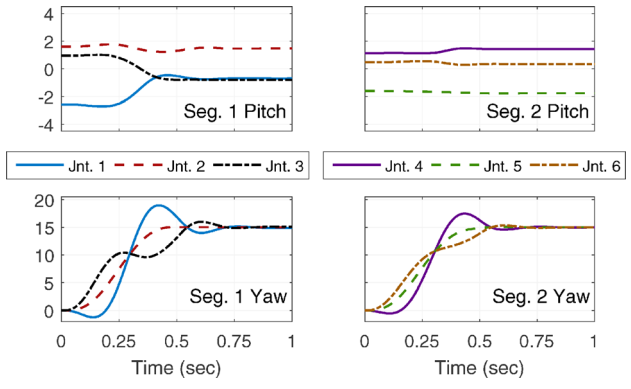

Fig. 9 Simulated joint angle trajectories for 90 deg yaw bending in 0.5 s (units: deg)

The orientation of the USRT base frame with respect to the load cell frame is shown in Fig. 6 and defined in Eq. (26)

$$\boldsymbol{R}_{\mathrm{TB}}^{\mathrm{LC}} = \begin{bmatrix} 0 & 0 & 1 \\ 0 & -1 & 0 \\ 1 & 0 & 0 \end{bmatrix} \tag{26}$$

Two types of loading will contribute to the force/moment loading between the USRT actuation module and ground: gravity and inertia. Given that both of these effects are modeled at the link COMs in Sec. 4, the position vector $\boldsymbol{p}_{i,\mathrm{COM}}^{\mathrm{TB}}$ (Eq. (3)) is used to relate this point to the USRT base/load cell frame origin. Equation (27) defines the force and moment applied on the USRT by the load cell, and the USRT applies an equal and opposite force/moment pair on the load cell

$$\begin{aligned} \boldsymbol{F}_{\mathrm{USRT}}^{\mathrm{LC}} &= \boldsymbol{R}_{\mathrm{TB}}^{\mathrm{LC}} \left(\sum_{i=0}^{6} \left(\boldsymbol{F}_{i,\mathrm{inr},B}^{\mathrm{TB}} - \boldsymbol{F}_{i,\mathrm{grv},B}^{\mathrm{TB}} \right) \right) \\ \boldsymbol{M}_{\mathrm{USRT}}^{\mathrm{LC}} &= \boldsymbol{R}_{\mathrm{TB}}^{\mathrm{LC}} \left(\sum_{i=0}^{6} \left(\boldsymbol{M}_{i,\mathrm{inr},B}^{\mathrm{TB}} + \tilde{\boldsymbol{p}}_{i,j,\mathrm{JC}}^{\mathrm{TB}} \left(\boldsymbol{F}_{i,\mathrm{inr},B}^{\mathrm{TB}} - \boldsymbol{F}_{i,\mathrm{grv},B}^{\mathrm{TB}} \right) \right) \right) \end{aligned} \tag{27}$$

The loading trajectories will be normalized with respect to the loading of the USRT when fully extended to emphasize how the USRT's loading changes due to the motion.

5.3 Loading Case Studies. Three case studies will be considered in this analysis: yaw-direction bending, pitch-direction bending, and bending through a rolling motion. For each of these case studies, a kinematic model will be used to derive desired cable trajectory inputs, which will be applied to the USRT's dynamic model. For planning the cable trajectories, it will be assumed that the six pitch and yaw angles in the robot are equal to φ_{des} and θ_{des}, respectively. However, individual joint angles in the USRT trajectories will not exactly match these desired joint angles, due to the variable effects of gravitational and elastic loading along the robot. Each case study below describes how its φ_{des} and θ_{des} trajectories are defined; using these trajectories, the kinematic model described in Sec. 4.1 is used to calculate $\delta_{\mathrm{des},j,k}$ using Eq. (10), for which $\boldsymbol{p}_{i,j,\mathrm{cbl}}^{i-1}$ is calculated using $\varphi_i = \varphi_{\mathrm{des}}$ and $\theta_i = \theta_{\mathrm{des}}$.

5.3.1 Yaw-Angle Bending. For yaw-angle bending, the joints' desired pitch angles $\varphi_{i,\mathrm{des}}$ are held fixed at 0 deg, and the joints' desired yaw angles are determined by prescribing a desired acceleration profile and integrating from initial positions/velocities.

The desired joint acceleration profile $\ddot{\theta}_{\mathrm{des}}$ is a sine wave defined for a single period T from time t_0 to t_f, as shown in Eq. (28), where A is the acceleration magnitude. Equation (29) defines A based on the desired initial $\theta_{\mathrm{des},0}$ and final $\theta_{\mathrm{des},f}$ yaw angles starting from an initial yaw velocity of $\dot{\theta}_{\mathrm{des},0}$. Trajectories for the yaw angle and velocity are calculated by integrating Eq. (28) from the initial conditions $\theta_{\mathrm{des},0}$ and $\dot{\theta}_{\mathrm{des},0}$

$$\ddot{\theta}_{\mathrm{des}} = \begin{cases} A \sin\left(2\pi(t - t_0)/T\right) & t_0 \le t \le t_f \\ 0 & t > t_f \end{cases} \tag{28}$$

$$A = 2\pi \left(\theta_{\mathrm{des},f} - \theta_{\mathrm{des},0} - \dot{\theta}_{\mathrm{des},0} T \right) \Big/ T^2 \tag{29}$$

The first set of simulations prescribes USRT bending of 90 deg in 0.3, 0.5, and 0.7 s, with trajectory parameters defined in Eq. (30). Figure 9 illustrates the joint trajectories associated with the $T = 0.5$ s trajectory. As previously discussed, the behavior in the pitch and yaw angles does not match the behavior planned for when generating the trajectory; the robot's dynamics cause variation in the joint angles along the length. For example, since the simulation parameters are taken from the experimental prototype discussed in Sec. 7, the pitch angles in segment 1 are not perfectly

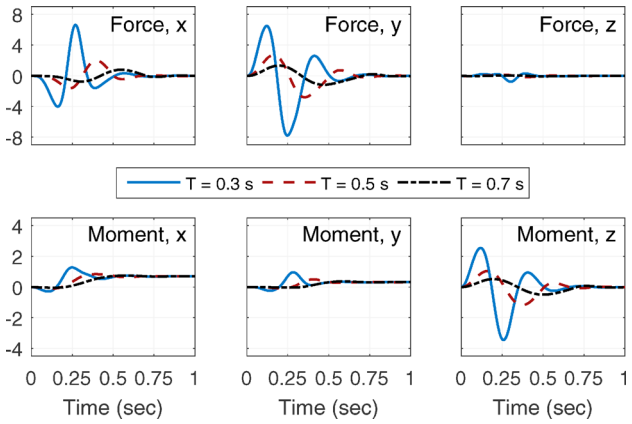

Fig. 10 Yaw-angle case study simulated loading: 90 deg bending (units: force: N; moment: N·m)

balanced such that their magnitudes are zero at the initial condition. However, the sum of these three angles does approximate zero within the segment. Despite these minor variations, the various joint angles track trajectories similar to those prescribed

$$\theta_{\text{des},0} = 0, \quad \theta_{\text{des},f} = 15\,\text{deg}, \quad \dot{\theta}_{\text{des},0} = 0, \quad T = \{0.3,\ 0.5,\ 0.7\} \tag{30}$$

Loading results for the three case studies are illustrated in Fig. 10. Negligible loading is observed in the $\boldsymbol{F}^{\text{LC}}_{\text{USRT}}$ z-component, due to the minimal change in the USRT's vertical COM position, whereas nontrivial loading is observed in the x- and y-components, due to the x- and y-direction USRT COM displacement. For the moment loading, minor steady-state variations in the x- and y-components of $\boldsymbol{M}^{\text{LC}}_{\text{USRT}}$ due to gravity are observed, but the most significant dynamic loading occurs in the z-component, as desired.

A second set of simulations is also performed for a net 150 deg bend in 0.5, 0.75, and 1.0 s; the trajectory parameters for these simulations are defined in Eq. (31). The 0.5 s case represents a similar effective velocity of the robot as the previous 0.3 s simulation (i.e., moving 90 deg in 0.3 s and moving 150 deg in 0.5 s both correspond to an effective velocity of 300 deg/s), which shows the impact of additional "stroke" on the dynamic loading

$$\theta_{\text{des},0} = 0, \quad \theta_{\text{des},f} = 25\,\text{deg}, \quad \dot{\theta}_{\text{des},0} = 0, \quad T = \{0.5,\ 0.75,\ 1.0\} \tag{31}$$

Figure 11 illustrates the loading results for these three cases. Qualitatively, the loading behavior is similar to the 90 deg yaw-bending loading, but with reduced magnitudes in the x- and y-components of $\boldsymbol{F}^{\text{LC}}_{\text{USRT}}$ and the z-component of $\boldsymbol{M}^{\text{LC}}_{\text{USRT}}$. Despite similar bending rates, the reduced time span in the 90 deg bending generates greater magnitude loading. In tail applications, higher-magnitude loading for a given yaw-direction displacement is beneficial for overcoming friction, as discussed in Ref. [28], whereas greater stroke is necessary for higher net rotation in the absence of friction. Future application-specific case studies will determine the optimal balance between these two considerations.

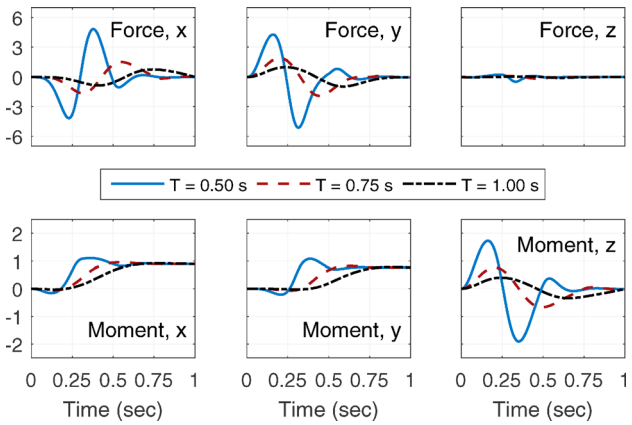

Fig. 11 Yaw-angle case study simulated loading: 150 deg bending (units: force: N; moment: N·m)

5.3.2 Pitch-Angle Bending. The trajectory planning for the pitch-angle bending is identical to that for yaw-angle bending except θ and φ are switched: θ_{des} is fixed at zero, and $\ddot{\varphi}_{\text{des}}$ is defined by Eq. (28). Likewise, two sets of simulations are carried out for the pitch-angle behavior of the robot using the same trajectories defined by the parameters in Eqs. (30) and (31), with φ substituted for θ. Unlike the yaw-direction motion, in which there was multidegree pitch motion due to variations in gravitational loading, there is no significant out-of-plane loading in this case to cause the yaw angles to vary during simulation (slight variations due to rounding errors do occur but are corrected for by the elastic loading of the compression spring). Therefore, only the pitch-angle trajectories, x- and z-components of $\boldsymbol{F}^{\text{LC}}_{\text{USRT}}$ and y-component of $\boldsymbol{M}^{\text{LC}}_{\text{USRT}}$ are shown.

Figure 12 illustrates the pitch-angle trajectories for the 90 deg USRT bending motion in 0.5 s. Due to the impact of changing gravitational loading as the robot bends, the similarity in joint trajectories within a given segment is less than the yaw-angle trajectories in Sec. 5.3.1. In the yaw case, the equal stiffness compression springs were the primary mechanism by which loading was balanced within a segment, and unequal inertia at the joints caused variation; in this pitch case, there is a more complex relationship between the effects of the compression springs, extension springs, gravity, and inertia, leading to greater variation within the segment.

Figure 13 illustrates the loading associated with the pitch direction case studies. Despite the reduced similarity of the joint angle trajectories in comparison to yaw-angle trajectories in Fig. 8, the loading profiles for the pitch motion are very similar to those for the yaw motion. The yaw and pitch force x-components correlate, as do the yaw force y-component and pitch force z-component; the yaw and pitch z- and y-components of moment are approximately equal and opposite. This shows a strong correlation between the planned kinematic trajectory and the applied loading, with the USRT dynamics merely perturbing the loading predicted by the applied kinematic trajectory. This feature will be further explored in future work related to task planning for the USRT.

5.3.3 Rolling Motion While Bending. To simulate the rolling motion depicted in Fig. 5, an alternative set of joint coordinates were used to plan the trajectory, which were then mapped into the desired pitch and yaw angle trajectories. The coordinates for which the alternative trajectory was defined were a desired bending plane angle κ_{des} and a bending angle β_{des} (analogous to β_i in Eq. (5)). The desired z-axis orientation is defined by the following equation:

$$\boldsymbol{z}^{i-1}_{\text{des}} = \boldsymbol{R}_Z(\kappa_{\text{des}})\boldsymbol{R}_Y(\beta_{\text{des}})\boldsymbol{z}^i_i \tag{32}$$

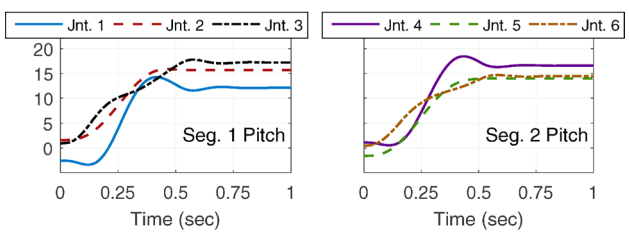

Fig. 12 Simulated pitch trajectories for 90 deg pitch bending in 0.5 s (units: deg)

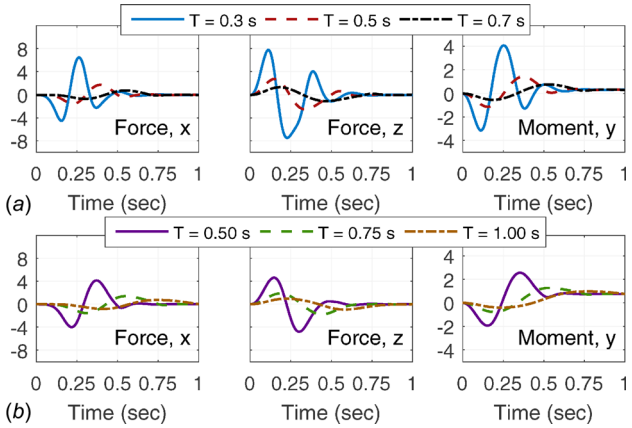

Fig. 13 Pitch-angle case study simulated loading: (*a*) 90 deg bend and (*b*) 150 deg bend (units: force: N; moment: N·m)

In these coordinates, the rolling motion is prescribed by holding β_{des} at a fixed value, while κ_{des} follows a trajectory matching θ_{des} from Sec. 5.3.1, from an initial angle of $\kappa_{\text{des},0}$ to a final angle of $\kappa_{des,f}$ starting from a velocity of $\dot{\kappa}_{\text{des},0}$, defined by Eqs. (28) and (29), for which κ is substituted for θ.

The angles κ_{des} and β_{des} are mapped into φ_{des} and θ_{des} using Eq. (33), where z_{des}^{i-1} is known as a function of κ_{des} and β_{des} from Eq. (32). The three transcendental equations in Eq. (33) may be uniquely solved for φ_{des} and θ_{des} in the domain $\{\varphi_{\text{des}}, \theta_{\text{des}}\} \in [-\beta_{\text{lim}}, \beta_{\text{lim}}]$

$$\boldsymbol{z}_{\text{des}}^{i-1} = \boldsymbol{R}_i^{i-1} \boldsymbol{z}_i^i \tag{33}$$

Three sets of simulations were run to analyze the impact of the initial bending angle on the loading generated by a −180 deg rolling motion at a fixed β_{des} of 15 deg. In the first set, the USRT was rolled from a zero-yaw, positive-pitch initial condition using the trajectory parameters in Eq. (34). In the second set, the USRT was rolled from a zero-pitch, negative-yaw initial condition using the trajectory parameters defined in Eq. (35). In the third set, the USRT was rolled from a zero-yaw, negative pitch initial condition using the trajectory parameters in Eq. (36)

$$\kappa_{\text{des},0} = 0\,\text{deg}, \quad \kappa_{\text{des},f} = -180\,\text{deg}, \quad \dot{\kappa}_{\text{des},0} = 0, \quad T = \{0.6, 0.8, 1.0\} \tag{34}$$

$$\kappa_{\text{des},0} = 90\,\text{deg}, \quad \kappa_{\text{des},f} = -90\,\text{deg}, \quad \dot{\kappa}_{\text{des},0} = 0, \quad T = \{0.6, 0.8, 1.0\} \tag{35}$$

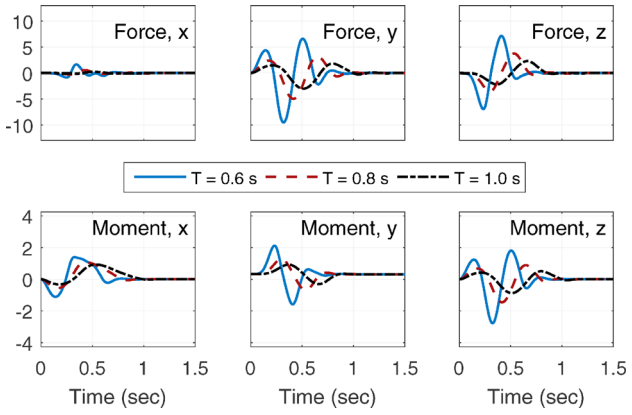

Fig. 14 Simulated loading for zero-yaw, positive-pitch initial condition for −180 deg rolling motion with 90 deg bend (units: force: N; moment: N·m)

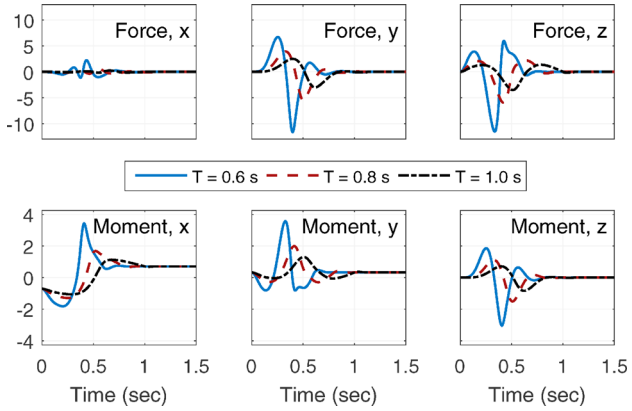

Fig. 15 Simulated loading for negative-yaw, zero-pitch initial condition for −180 deg rolling motion with 90 deg bend (units: force: N; moment: N·m)

$$\kappa_{\text{des},0} = 180\,\text{deg}, \quad \kappa_{\text{des},f} = 0\,\text{deg}, \quad \dot{\kappa}_{\text{des},0} = 0, \quad T = \{0.6, 0.8, 1.0\} \tag{36}$$

Figures 14–16 show the loading for the three sets of roll motion simulations. In each case, the x-component of $\boldsymbol{F}_{\text{USRT}}^{\text{LC}}$ is minimal, as the USRT COM is not prescribed motion in this direction (dynamic effects during the robot's motion introduce slight x-coordinate motions which cause slight perturbations in this loading). Given that all three trajectories consist of a clockwise, −180 deg rotation of the USRT COM, the dynamic components of the $\boldsymbol{M}_{\text{USRT}}^{\text{LC}}$ x-component of the three figures are similar. However, variations are caused by the fact that for the zero-initial pitch case, since the initial and final configurations bend away from the x–z plane, there are nonzero static offsets for the loading. In addition, the variation in how the robot must act with or against gravity for different initial angles changes the magnitude of the loading generated by each motion.

The loading trajectories of the $\boldsymbol{F}_{\text{USRT}}^{\text{LC}}$ and $\boldsymbol{M}_{\text{USRT}}^{\text{LC}}$ y- and z-components for Fig. 16 are of opposite sign than those of Fig. 14, given that the two motions move in opposite vertical directions. However, the magnitudes of these trajectories are not equal, due to the effect of gravity acting with the robot's motion in Fig. 14 and against the robot's motion in Fig. 16. In terms of acceleration, for Fig. 14, gravity acts against acceleration and with deceleration; for Fig. 16, gravity acts with acceleration and against deceleration. However, for Fig. 15, both acceleration and deceleration act against gravity; this leads to the highest magnitude peak loading for each of the four components under consideration. This

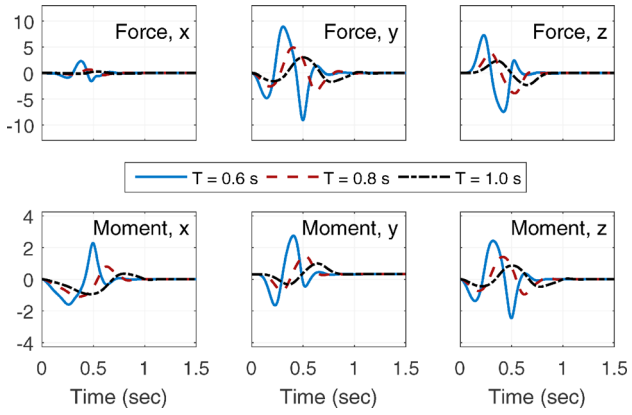

Fig. 16 Simulated loading for zero-yaw, negative-pitch initial condition for −180 deg rolling motion with 90 deg bend (units: force: N; moment: N·m)

shows that $\kappa_{\text{des},0}$ provides a means to adjust the secondary loading the USRT applies during a rolling motion; for a given roll, $\kappa_{\text{des},0}$ may be chosen such that the y- and z-components of force and moment do not destabilize the robot in addition to applying the desired x-axis moment. However, unlike the previous two case studies, the loading generated by the rolling USRT motion generates yaw, pitch, and roll moment loading of comparable magnitude, requiring greater consideration of the destabilizing effects of the pitch and yaw moments during a roll motion.

6 Sensing and State Estimation

This section highlights the two types of sensing incorporated into the USRT design for state estimation: six pairs of linear displacement sensors for universal joint angle estimation (Sec. 6.1) and seven inertial measurement units for joint velocity estimation (Sec. 6.2).

6.1 Joint Angle Estimation. Figure 17(*a*) illustrates two joints of the USRT with two pairs of distance sensors. To accommodate the sensors in each subsegment, the sensors are alternatively placed "above" and "below" the universal joint along the robot. In both configurations, the position vectors from the disk center to the center of the sensor mount are at 45 deg angles with respect to the disk's vertical $\boldsymbol{x}_i$–$\boldsymbol{z}_i$ plane, ensuring a 90 deg separation of the sensor pair, which maximizes the sensor fidelity within the subsegment workspace.

The joint i sensor pair is mounted to link $i-1$ with a universal joint and to link i with a spherical joint, shown in Fig. 4, to ensure fixed sensor endpoint positions with respect to the two disks without overconstraining the sensor.

For joint i's sensor j, the forward kinematics (calculating the distance $d_{i,j,\text{sns}}$ between the sensor's anchor points from φ_i and θ_i) are calculated using the positions from the sensor j base to joint i ($\boldsymbol{p}^{i-1}_{i,j,\text{SJ}}$) and from joint i to the sensor j tip ($\boldsymbol{p}^{i}_{i,j,\text{JS}}$), defined in Eq. (37), where $\boldsymbol{p}^{i-1}_{i,j,\text{sns},B}$ is the position from the link $i-1$ disk center to the sensor j base and $\boldsymbol{p}^{i}_{i,j,\text{sns},T}$ is the position from the link i disk center to the sensor j tip. The position $\boldsymbol{p}^{i-1}_{i,j,\text{sns}}$ from the sensor j base to tip is defined in Eq. (38), along with $d_{i,j,\text{sns}}$

$$\boldsymbol{p}^{i-1}_{i,j,\text{SJ}} = -\boldsymbol{p}^{i-1}_{i,j,\text{sns},B} + L_{\text{DJ}}\boldsymbol{z}, \quad \boldsymbol{p}^{i}_{i,j,\text{JS}} = L_{\text{JD}}\boldsymbol{z} + \boldsymbol{p}^{i}_{i,j,\text{sns},T} \tag{37}$$

$$\boldsymbol{p}^{i-1}_{i,j,\text{sns}} = \boldsymbol{p}^{i-1}_{i,j,\text{SJ}} + \boldsymbol{R}^{i-1}_{(i-1)i}\boldsymbol{p}^{i}_{i,j,J2S}, \quad d_{i,j,\text{sns}} = \|\boldsymbol{p}^{i-1}_{i,j,\text{sns}}\| \tag{38}$$

To analytically calculate the inverse kinematics, further constraints on the sensor geometry are necessary, as defined in Eq. (39): (i) the disk-frame z-coordinate displacement between the sensor j base and joint i is zero, (ii) the disk-frame sensor base and tip x-coordinates are equal, and (iii) the disk-frame sensor base and tip y-coordinates are equal

$$\left(\boldsymbol{z}^{i-1}_{i-1}\right)^T\boldsymbol{p}^{i-1}_{i,j,\text{SJ}} = 0, \quad \begin{matrix}\left(\boldsymbol{x}^{i-1}_{i-1}\right)^T\boldsymbol{p}^{i-1}_{i,j,\text{SJ}} = \left(\boldsymbol{x}^{i}_{i}\right)^T\boldsymbol{p}^{i}_{i,j,\text{JS}},\\ \left(\boldsymbol{y}^{i-1}_{i-1}\right)^T\boldsymbol{p}^{i-1}_{i,j,\text{SJ}} = \left(\boldsymbol{y}^{i}_{i}\right)^T\boldsymbol{p}^{i}_{i,j,\text{JS}}\end{matrix} \tag{39}$$

With these constraints, an analytical formulation for the pitch and yaw angles may be found by considering the disk i sensor frame i,S shown in Fig. 17(*b*). These frames are generated by rotating the disk i frame by -45 deg about the $\boldsymbol{z}_i$-axis. The positions $\boldsymbol{p}_{i,j,\text{SJ}}$ and $\boldsymbol{p}_{i,j,\text{JS}}$ are defined with respect to frames $i-1$, S, and i,S, respectively, using Eq. (40), where r_S is the sensor mounting radius, shown in Fig. 17(*b*), and L_S is the zero-angle sensor length, shown in Fig. 17(*a*). The $(-1)^i$ term accounts for the alternating placement of the sensors above and below the universal joint

$$\boldsymbol{p}^{i-1,S}_{i,j,\text{SJ}} = \begin{cases}(-1)^i r_S \boldsymbol{y}^{i-1,S}_{i-1,S}, & j=1\\ (-1)^i r_S \boldsymbol{x}^{i-1,S}_{i-1,S}, & j=2\end{cases}$$
$$\boldsymbol{p}^{i,S}_{i,j,\text{JS}} = \begin{cases}(-1)^i r_S \boldsymbol{y}^{i,S}_{i,S} + L_S \boldsymbol{z}^{i,S}_{i,S}, & j=1\\ (-1)^i r_S \boldsymbol{x}^{i,S}_{i,S} + L_S \boldsymbol{z}^{i,S}_{i,S}, & j=2\end{cases} \tag{40}$$

A new relative orientation matrix $\boldsymbol{R}^{i-1,S}_{i,S}$ between frames $i-1$,S and i,S is defined in Eq. (41), where ρ_i and γ_i are the joint i sensor-frame pitch and yaw angles, respectively. Using this rotation matrix, a formulation for the sensor position $\boldsymbol{p}^{i-1,S}_{i,j,\text{sns}}$ from base to tip may be formulated using Eq. (42)

$$\boldsymbol{R}^{i-1,S}_{i,S} = \boldsymbol{R}_Y(\rho_i)\boldsymbol{R}_X(\gamma_i) \tag{41}$$

$$\boldsymbol{p}^{i-1,S}_{i,j,\text{sns}} = \boldsymbol{p}^{i-1,S}_{i,j,\text{SJ}} + \boldsymbol{R}^{i-1,S}_{i,S}\boldsymbol{p}^{i,S}_{i,j,\text{SJ}} \tag{42}$$

The scalar sensor distances $d_{i,j,\text{sns}}$ are invariant to the frame in which the sensor position vectors are expressed, enabling expression of $d_{i,j,\text{sns}}$ in terms of ρ_i and γ_i. Equations (43) and (44) expand $\|\boldsymbol{p}^{i-1,S}_{i,j,\text{sns}}\|^2$ for sensors 1 and 2. Because Eq. (44) is solely a function of γ_i, it may be solved for uniquely in the domain $\gamma_i \in (-90, 90)$ deg. Using this value for γ_i in Eq. (43), ρ_i may also be calculated uniquely in the domain $\rho_i \in (-90, 90)$ deg

$$\|\boldsymbol{p}^{i-1,S}_{i,1,\text{sns}}\|^2 = d^2_{i,1,\text{sns}} = 2r_S^2 + L_S^2 - 2r_S^2 c_{\psi i} - 2r_S L_S s_{\psi i} c_{\gamma i} \tag{43}$$

$$\|\boldsymbol{p}^{i-1,S}_{i,2,\text{sns}}\|^2 = d^2_{i,2,\text{sns}} = 2r_S^2 + L_S^2 - 2r_S^2 c_{\gamma i} + 2r_S L_S s_{\gamma i} \tag{44}$$

The joint angles ρ_i and γ_i may be mapped into φ_i and θ_i by equating implicit formulations of the z-axes of frames $\boldsymbol{R}^{i-1}_{i}$ and $\boldsymbol{R}^{i-1,S}_{i,S}$, as shown in the below equation:

$$\boldsymbol{R}^{i-1}_{i-1,S}\boldsymbol{R}^{i-1,S}_{i,S}\boldsymbol{z}^{i,S}_{i,S} = \boldsymbol{R}^{i-1}_{i}\boldsymbol{z}^{i}_{i} \rightarrow \boldsymbol{R}_Z(-45^\circ)\boldsymbol{R}^{i-1,S}_{i,S}\boldsymbol{z}^{i,S}_{i,S} = \boldsymbol{R}^{i-1}_{i}\boldsymbol{z}^{i}_{i} \tag{45}$$

6.2 Joint Velocity Estimation. The link i IMU measures the link i angular velocity vector $\boldsymbol{\omega}^i_i$ with respect to the link-fixed frame i. Using the estimated relative orientation $\boldsymbol{R}^{i-1}_{i}$ from the joint angle estimate (Sec. 6.1), $\boldsymbol{\omega}^{i-1}_{(i-1)i}$ may be calculated using Eq. (46) as the joint i relative angular velocity between links $i-1$ and i

$$\boldsymbol{\omega}^{i-1}_{(i-1)i} = \boldsymbol{R}^{i-1}_{i}\boldsymbol{\omega}^{i}_{i} - \boldsymbol{\omega}^{i-1}_{i-1} \tag{46}$$

Based on Eq. (4), $\dot{\varphi}_i$ and $\dot{\theta}_i$ may be extracted from $\boldsymbol{\omega}^{i-1}_{(i-1)i}$, as shown in Eq. (47), due to the orthogonality of $\boldsymbol{y}^{i-1}_{i-1}$ and $\boldsymbol{R}^{i-1}_{i}\boldsymbol{x}^{i}_{i}$

$$\dot{\varphi}_i = \left(\boldsymbol{y}^{i-1}_{i-1}\right)^T\boldsymbol{\omega}^{i-1}_{(i-1)i}, \quad \dot{\theta}_i = \left(\boldsymbol{R}^{i-1}_{i}\boldsymbol{x}^{i}_{i}\right)^T\boldsymbol{\omega}^{i-1}_{(i-1)i} \tag{47}$$

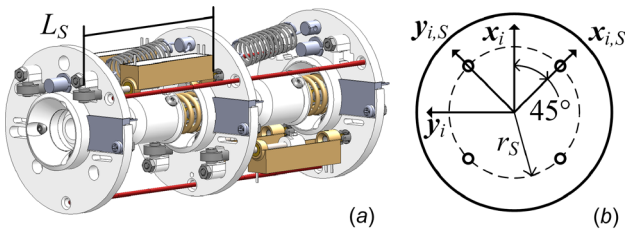

Fig. 17 USRT sensing: (*a*) displacement sensor arrangement in adjacent subsegments and (*b*) disk *i* sensor-frame definition

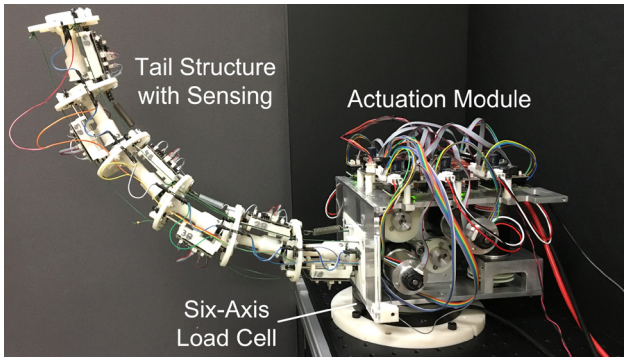

Fig. 18 USRT experimental test platform

7 Experimental Results

This section describes the integration and testing of the prototype USRT. Simulations from the three case studies described in Sec. 5 are implemented on the prototype, and the loading is measured and compared to the predicted loading.

7.1 Universal Spatial Robotic Tail Implementation. Figure 18 shows the USRT experimental test platform. Structural components of the robot were made of thermoplastic using a Stratasys uPrint 3D printer and were connected by commercial universal joints from SDP/SI (Molded Universal Joints, 3/8 in OD with 3/16 in Bore Insert, part #A-5Z-8-D306). Commercial compression and extension springs with properties defined in Tables 1 and 2 were utilized, and spring anchor positions were adjusted so that the USRT is extended (approximately straight) in the absence of actuation.

Six brushless EC-i 40 Maxon motors (36 V) were used to actuate the prototype: three 100 W brushless motors for segment 1 (part #496661) and three 70 W motors for segment 2 (part #496655). Segment 1 motors are higher power than segment 2 motors due to the increased inertial loading at segment 1 joints due to the presence of segment 2. Gear reductions (15:1 for segment 1 and 26:1 for segment 2) and cable spool diameters (34 mm for segment 1 and 49 mm for segment 2) were chosen so that the USRT would be capable of bending from 0 to 180 deg in 0.25 s without exceeding the motors' velocity limits. The gear reduction and spool diameter were chosen to accomplish this goal with maximum gear ratio and minimum spool diameter, to maximize the force the cable can support given the motor's torque limitations.

The USRT's motors were controlled by six ESCON 50/5 Maxon motor drivers operating in closed-loop velocity control mode. Sensor feedback for each motor control loop is a U.S. Digital Miniature Optical Kit Encoder (part #E4T-360-236-DHMB) mounted to the motor shaft. For the desired motor inputs, LabVIEW generated 15 byte packets containing motor speeds and power states at 10 ms intervals (100 Hz) and sent these to an ARM Cortex M4 microcontroller that interfaces with the six motor drivers. The USRT was powered using a 37 V LiPo battery connected to the motors drivers through a custom power regulator.

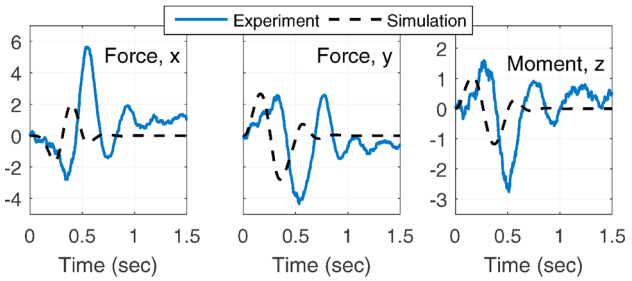

Fig. 20 Simulated and experimental loading for yaw case study 90 deg bend in 0.5 s (units: force: N; moment: N·m)

7.2 Universal Spatial Robotic Tail Loading Results. Loading results were generated using trajectories considered in the three case studies analyzed in Sec. 5.3. Measured results were filtered using the MATLAB "filter" function to implement a moving-average filter, with a window size of 50 samples for samples recorded at approximately 400 Hz, and the simulated and experimental trajectories were synchronized at the initiation of each trajectory. As with the simulated loading, the results shown are normalized to the measured loading of the USRT in its initially extended configuration. In addition, the USRT's motion is initiated after at least 50 samples have been measured, so that the filter has sufficient samples preceding the dynamic loading profile to effectively filter.

For the yaw-angle case study, the USRT was driven through a 90 deg bend in 0.5 s. The measured joint trajectories and loading are shown in Figs. 19 and 20, along with the simulated results from Sec. 5.3.1. Although the simulations approximate the general pattern of the results, there are variations in the joint trajectories and loading. For the joint trajectories, the implementation of the compression spring mounting leads to slight yaw variations along the length of the robot in its nominally straight configuration (i.e., zero cable displacement), as evidenced by the nonzero initial joint angles in Fig. 19. The next generation of USRT will modify the compression spring mounting design to reduce these undesired initial yaw angle variations.

Greater overshoot and vibration is also seen in the experimental results (both joint trajectories and loading) than the simulated

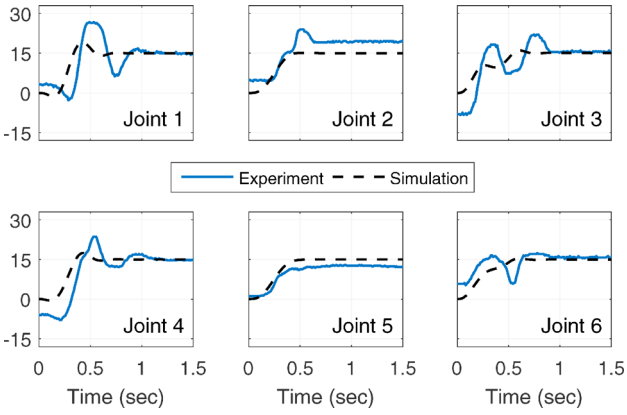

Fig. 19 Simulated and experimental joint trajectories for yaw case study 90 deg bend in 0.5 s (units: deg)

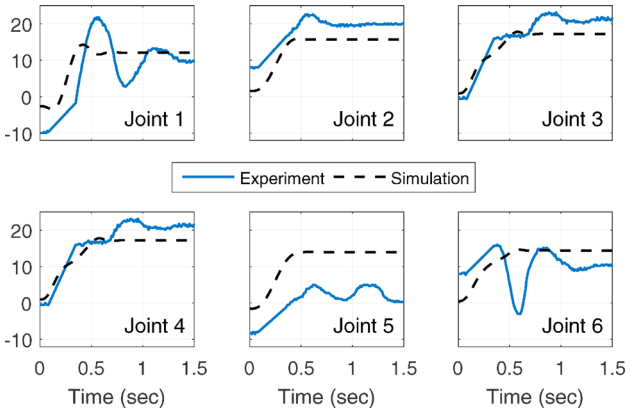

Fig. 21 Simulated and experimental joint trajectories for pitch case study 90 deg bend in 0.5 s (units: deg)

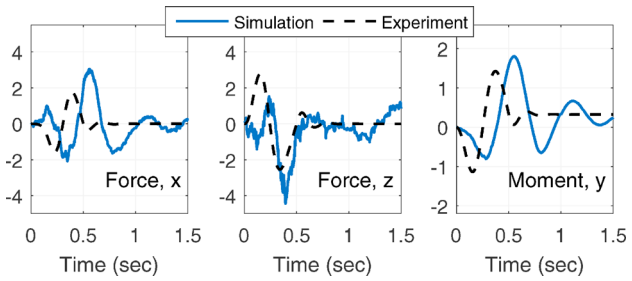

Fig. 22 Simulated and experimental loading for pitch case study 90 deg bend in 0.5 s (units: force: N; moment: N·m)

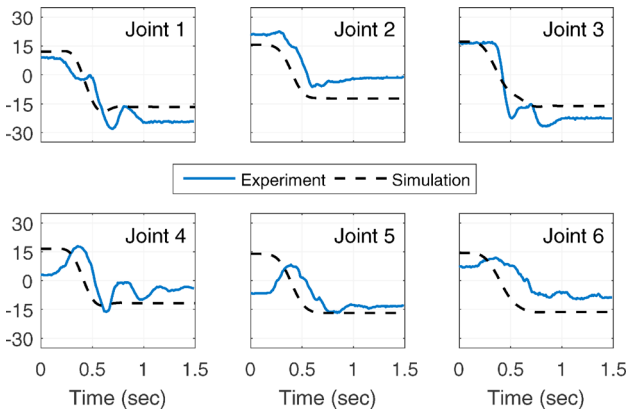

Fig. 23 Simulated and experimental pitch-angle trajectories for roll case study 180 deg roll at a 90 deg bend in 0.8 s (units: deg)

results. As discussed in Ref. [8], the cable tension profiles during dynamic motion vary greatly due to the need to accelerate and decelerate the robot during a motion. Because the motor controller generates spool torque/cable tension based on prescribed velocity inputs, the controller cannot anticipate the highly dynamic changes in torque requirements to match the desired trajectory. Thus, more advanced control of the system, in which motor torques (or, interchangeably, motor currents) are prescribed to the motor driver instead of velocity commands implemented using a closed loop. The inclusion of a feedforward control component in this controller will also help with the lag observed in Fig. 20; given that the motor velocity controller only utilizes feedback to prescribe motor current, a lag is necessary to generate sufficient error to generate a sufficient current signal to actuate the motor.

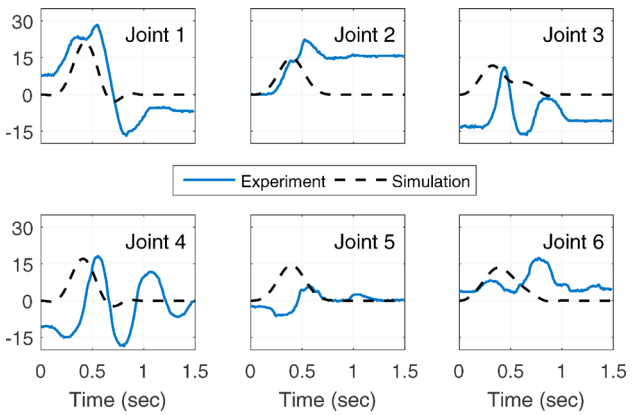

Fig. 24 Simulated and experimental yaw-angle trajectories for roll case study 180 deg roll at a 90 deg bend in 0.8 s (units: deg)

For the pitch-angle case study, the USRT was driven through a 90 deg bend in 0.5 s. The measured joint trajectories and loading are shown in Figs. 21 and 22, along with the simulated results from Sec. 5.3.2. The experimental joint angle trajectories show variations from the simulated trajectories similar to those for the yaw-bending case study, but with higher-magnitude vertical offset from the desired trajectories. For the yaw-direction bending, the compression spring is the primary means of distributing loading. However, in this pitch-direction motion, particularly in joints close to the base, the extension spring plays a similar or greater role in the dynamics than the compression spring. Furthermore, this variation in elastic loading along the length, while necessary for minimizing the actuation for supporting the USRT in its cantilevered-mode, reduces the uniformity in bending along the robot.

Although the pitch-motion joint trajectories show greater variation from their nominal values than the yaw-motion joint trajectories, the loading in Fig. 22 shows greater correlation to the predicted loading than the yaw-motion loading. Because the robot is moving against gravity, gravity will help decelerate the USRT, reducing the overshoot in the loading compared to the yaw-direction bending. As before, the measured trajectories exhibit lag and increase oscillation in comparison to the simulated values due to the inner-loop motor velocity controller; a torque/current controller that utilizes both feedforward and feedback control elements is planned in future work to reduce these variations. Minor variations are observed in the USRT's yaw-angle trajectories, $\boldsymbol{F}^{\mathrm{LC}}_{\mathrm{USRT}}$ y-component, and $\boldsymbol{M}^{\mathrm{LC}}_{\mathrm{USRT}}$ x- and z-component, due to the nonzero initial yaw-angle configuration, as discussed for the yaw-direction case study. However, the magnitudes of these effects are secondary in comparison to those shown in Fig. 22.

For the roll angle case study, the USRT was driven through a −180 deg rolling motion at a prescribed bend of 90 deg in 0.5 s starting from zero yaw angle and positive pitch. The measured joint trajectories and loading are shown in Figs. 23–25, along with simulated results from Sec. 5.3.3. The joint trajectories show significant variations from their predicted value, due to the simultaneous, highly dynamic variation of pitch and yaw during the motion. In addition, since the trajectory did not start from the nominally straight configuration, additional errors were introduced in the positioning of the USRT into the initial configuration. Despite these errors, the correlation between the measured and predicted loading is the strongest among the three case studies. Because the USRT is not moving monotonically in a single direction, there is less accumulated velocity that leads to overshoot. The most significant variation is in the $\boldsymbol{F}^{\mathrm{LC}}_{\mathrm{USRT}}$ x-component, due to unmodeled motion of the robot's COM along the x-axis. It is likely that controller improvements will lead to stable higher

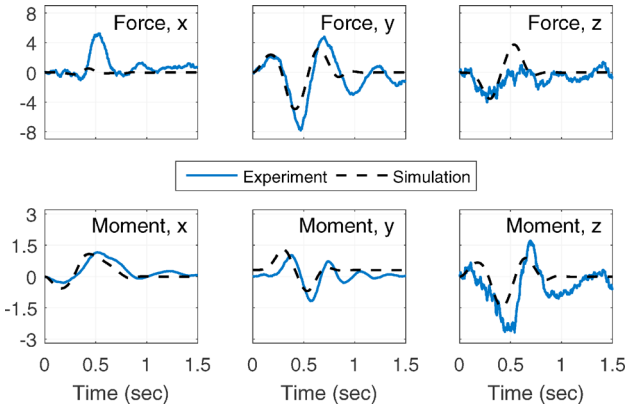

Fig. 25 Simulated and experimental loading for roll case study 180 deg roll at a 90 deg bend in 0.8 s (units: force: N; moment: N·m)

speed motions being possible, improving the loading capacity of the USRT.

The results presented in this section do not represent the maximum capacity of the USRT itself. They demonstrate the functional capabilities of the USRT, but future work focusing on the control of this class of robot will enable higher speed motions with higher mass, both of which correlate to higher-magnitude loading.

8 Conclusion

This paper has presented the novel design of a hyperredundant robot capable of dynamic spatial motion in multiple actuated segments. Elastic springs are used to both resolve the redundancy within an actuated segment and help to counteract undesired gravitational sag in the cantilevered structure. The design of the system is presented, along with a mechanical model of the system capable of predicting the robot's trajectory given a set of cable displacement inputs. Integrated sensing capable of measuring the robot's joint angles and joint velocities in real-time is also demonstrated. Simulations are generated showing the USRT's workspace and the loading associated yaw, pitch, and roll motions of the USRT, and an experimental platform is integrated to compare the simulated loading to measured results.

Future work will include a more detailed analysis of the control of the USRT in relation to the primary target application: stabilizing and maneuvering legged robots. Inverse dynamics-based analysis will generate feedforward torque commands for the motor to anticipate the loading required in the cables to move the USRT through a desired trajectory. These inputs will be coupled with a feedback controller to modify these torque trajectories to track the desired USRT configuration. Given a legged robot, optimizations for determining the proper mass and mass distribution of the USRT will also be performed. Furthermore, beyond its use as a robotic tail, studies will be performed to analyze how the underlying design of the USRT could be used in applications such as aquatic propulsion (octopuslike tentacles and fishlike tails), energy harvesting (capturing passive motion using a flexible structure), aerospace robots (using flexible structures to maneuvering satellites), and snakelike ground propulsion.

Acknowledgment

The authors would like to thank Anil Kumar for his assistance with the electrical design of the USRT.

Funding Data

- This material is based upon work supported by the National Science Foundation (Grant No. 1557312).

References

[1] O'Connor, S. M., Dawson, T. J., Kram, R., and Donelan, J. M., 2014, "The Kangaroo's Tail Propels and Powers Pentapedal Locomotion," Biol. Lett., **10(7)**, p. 20140381.

[2] Sfakiotakis, M., Lane, D. M., and Davies, J. B. C., 1999, "Review of Fish Swimming Modes for Aquatic Locomotion," IEEE J. Oceanic Eng., **24**(2), pp. 237–252.

[3] Fish, F. E., Bostic, S. A., Nicastro, A. J., and Beneski, J. T., 2007, "Death Roll of the Alligator: Mechanics of Twist Feeding in Water," J. Exp. Biol., **210**(Pt. 16), pp. 2811–2818.

[4] Wilson, A. M., Lowe, J. C., Roskilly, K., Hudson, P. E., Golabek, K. A., and McNutt, J. W., 2013, "Locomotion Dynamics of Hunting in Wild Cheetahs," Nature, **498**(7453), pp. 185–189.

[5] Walker, C., Vierck, C. J., Jr., and Ritz, L. A., 1998, "Balance in the Cat: Role of the Tail and Effects of Sacrocaudal Transection," Behav. Brain Res., **91**(1–2), pp. 41–47.

[6] Young, J. W., Russo, G. A., Fellmann, C. D., Thatikunta, M. A., and Chadwell, B. A., 2015, "Tail Function During Arboreal Quadrupedalism in Squirrel Monkeys (*Saimiri Boliviensis*) and Tamarins (*Saguinus Oedipus*)," J. Exp. Zool., Part A, **323**(8), pp. 556–566.

[7] Mallison, H., 2010, "CAD Assessment of the Posture and Range of Motion of Kentrosaurus Aethiopicus Hennig 1915," Swiss J. Geosci., **103**(2), pp. 211–233.

[8] Rone, W. S., Saab, W., and Ben-Tzvi, P., 2017, "Design, Modeling and Optimization of the Universal-Spatial Robotic Tail," ASME Paper No. IMECE2017-71463.

[9] Saab, W., Rone, W. S., and Ben-Tzvi, P., 2018, "Discrete Modular Serpentine Robotic Tail: Design, Analysis and Experimentation," Robotica, in press.

[10] Saab, W., Rone, W. S., Kumar, A., and Ben-Tzvi, P., 2018, "Design and Integration of a Novel Spatial Articulated Robotic Tail," IEEE/ASME Trans. Mechatronics, in press.

[11] Saab, W., Rone, W. S., and Ben-Tzvi, P., 2017, "Robotic Modular Leg: Design, Analysis and Experimentation," ASME J. Mech. Rob., **9**(2), p. 024501.

[12] Jin, J., Ko, S., and Ryoo, C. K., 2008, "Fault Tolerant Control for Satellites With Four Reaction Wheels," Control Eng. Pract., **16**(10), pp. 1250–1258.

[13] Machairas, K., and Papadopoulos, E., 2015, "On Quadruped Attitude Dynamics and Control Using Reaction Wheels and Tails," European Control Conference (ECC), Linz, Austria, July 15–17, pp. 753–758.

[14] Kim, B., Kim, D.-H., Jung, J., and Park, J.-O., 2005, "A Biomimetic Undulatory Tadpole Robot Using Ionic Polymer–Metal Composite Actuators," Smart Mater. Struct., **14**(6), pp. 1579–1585.

[15] Kopman, V., Laut, J., Acquaviva, F., Rizzo, A., and Porfiri, M., 2014, "Dynamic Modeling of a Robotic Fish Propelled by a Compliant Tail," IEEE J. Oceanic Eng., **40**(1), pp. 209–221.

[16] Briggs, R., Lee, J., Haberland, M., and Kim, S., 2012, "Tails in Biomimetic Design: Analysis, Simulation, and Experiment," IEEE/RSJ International Conference on Intelligent Robots and Systems (IROS), Vilamoura, Portugal, Oct. 7–12, pp. 1473–1480.

[17] Patel, A., and Braae, M., 2014, "Rapid Acceleration and Braking: Inspiration From the Cheetah's Tail," IEEE International Conference on Robotics and Automation (ICRA), Hong Kong, China, May 31–June 7, pp. 793–799.

[18] Libby, T., Moore, T. Y., Chang-Siu, E., Li, D., Cohen, D. J., Jusufi, A., and Full, R. J., 2012, "Tail-Assisted Pitch Control in Lizards, Robots and Dinosaurs," Nature, **481**(7380), pp. 181–184.

[19] Berenguer, F. J., and Monasterio-Huelin, F. M., 2008, "Zappa: A Quasi-Passive Biped Walking Robot With a Tail: Modeling, Behavior, and Kinematic Estimation Using Accelerometers," IEEE Trans. Ind. Electron., **55**(9), pp. 3281–3289.

[20] Casarez, C., Penskiy, I., and Bergbreiter, S., 2013, "Using an Inertial Tail for Rapid Turns on a Miniature Legged Robot," IEEE International Conference on Robotics and Automation (ICRA), Karlsruhe, Germany, May 6–10, pp. 5469–5474.

[21] Kohut, N. J., Haldane, D. W., Zarrouk, D., and Fearing, R. S., 2012, "Effect of Inertial Tail on Yaw Rate of 45 Gram Legged Robot," International Conference on Climbing and Walking Robots and the Support Technologies for Mobile Machines, Baltimore, MD, July 23–26, pp. 157–164.

[22] He, G., and Geng, Z., 2009, "Exponentially Stabilizing an One-Legged Hopping Robot With Non-SLIP Model in Flight Phase," Mechatronics, **19**(3), pp. 364–374.

[23] Patel, A., and Braae, M., 2013, "Rapid Turning at High-Speed: Inspirations From the Cheetah's Tail," IEEE/RSJ International Conference on Intelligent Robots and Systems (ICRA), Tokyo, Japan, Nov. 3–7, pp. 5506–5511.

[24] Chang-Siu, E., Libby, T., Brown, M., Full, R. J., and Tomizuka, M., 2013, "A Nonlinear Feedback Controller for Aerial Self-Righting by a Tailed Robot," IEEE International Conference on Robotics and Automation (ICRA), Karlsruhe, Germany, May 6–10, pp. 32–39.

[25] Ikeda, F., and Toyama, S., 2015, "A Proposal of Right and Left Turning Mechanism for Quasi-Passive Walking Robot," IEEE International Conference on Advanced Robotics and Intelligent Systems (ARIS), Taipei, Taiwan, May 29–31, pp. 1–5.

[26] Mutka, A., Orsag, M., and Kovacic, Z., 2013, "Stabilizing a Quadruped Robot Locomotion Using a Two Degree of Freedom Tail," 21st Mediterranean Conference on Control and Automation (MED), Chania, Greece, June 25–28, pp. 1336–1342.

[27] Provancher, W. R., Jensen-Segal, S. I., and Fehlberg, M. A., 2011, "ROCR: An Energy-Efficient Dynamic Wall-Climbing Robot," IEEE/ASME Trans. Mechatronics, **16**(5), pp. 897–906.

[28] Rone, W. S., and Ben-Tzvi, P., 2016, "Dynamic Modeling and Simulation of a Yaw-Angle Quadruped Maneuvering With a Robotic Tail," ASME J. Dyn. Syst. Meas. Control, **138**(8), p. 084502.

[29] Rone, W. S., and Ben-Tzvi, P., 2014, "Continuum Robotic Tail Loading Analysis for Mobile Robot Stabilization and Maneuvering," ASME Paper No. DETC2014-34678.

[30] Robinson, G., and Davies, J. B. C., 1999, "Continuum Robots: A State of the Art," IEEE International Conference on Robotics and Automation, Detroit, MI, May 10–15, pp. 2849–2854.

[31] McMahan, W., Chitrakaran, V., Csencsits, M. A., Dawson, D. M., Walker, I. D., Jones, B. A., Pritts, M., Dienno, D., Grissom, M., and Rahn, C. D., 2006, "Field Trials and Testing of the OctArm Continuum Manipulator," IEEE International Conference on Robotics and Automation (ICRA), Orlando, FL, May 15–19, pp. 2336–2341.

[32] Mazzolai, B., Margheri, L., Cianchetti, M., Dario, P., and Laschi, C., 2012, "Soft-Robotic Arm Inspired by the Octopus: II. From Artificial Requirements to Innovative Technological Solutions," Bioinspiration Biomimetics, **7**(2), p. 25005.

[33] Festo, 2010, "Bionic Handling Assistant," Festo, Esslingen, Germany, accessed Mar. 16, 2018, http://www.festo.com/net/SupportPortal/Files/42050/Brosch_FC_BHA_3_0_EN_lo.pdf

[34] Rone, W. S., and Ben-Tzvi, P., 2014, "Continuum Robot Dynamics Utilizing the Principle of Virtual Power," IEEE Trans. Rob., **30**(1), pp. 275–287.
[35] Rone, W. S., and Ben-Tzvi, P., 2014, "Mechanics Modeling of Multisegment Rod-Driven Continuum Robots," ASME J. Mech. Rob., **6**(4), p. 041006.
[36] Wei, W., Xu, K., and Simaan, N., 2006, "A Compact Two-Armed Slave Manipulator for Minimally Invasive Surgery of the Throat," IEEE/RAS-EMBS International Conference on Biomedical Robotics and Biomechatronics (BioRob), Pisa, Italy, Feb. 20–22, pp. 769–774.
[37] Yim, M., 1994, *Locomotion With a Unit-Modular Reconfigurable Robot*, Stanford University, Stanford, CA.
[38] Arai, M., Tanaka, Y., Hirose, S., Kuwahara, H., and Tsukui, S., 2008, "Development of 'Souryu-IV' and 'Souryu-V:' Serially Connected Crawler Vehicles for In-Rubble Searching Operation," J. Field Rob., **25**(1–2), pp. 31–65.
[39] Shammas, E., Wolf, A., Brown, H., Ben, J., and Choset, H., 2003, "New Joint Design for Three-Dimensional Hyper Redundant Robots," IEEE/RSJ International Conference on Intelligent Robots and Systems (IROS), Las Vegas, NV, Oct. 27–31, pp. 3594–3599.
[40] Wolf, A., Brown, H. B., Casciola, R., Costa, A., Schwerin, M., Shamas, E., and Choset, H., 2003, "A Mobile Hyper Redundant Mechanism for Search and Rescue Tasks," IEEE/RSJ International Conference on Intelligent Robots and Systems (IROS), Las Vegas, NV, Oct. 27–31, pp. 2889–2895.
[41] Li, Z., and Du, R., 2013, "Design and Analysis of a Bio-Inspired Wire-Driven Multi-Section Flexible Robot," Int. J. Adv. Rob. Syst., **10**(4), p. 209.
[42] Suh, J. W., Kim, K. Y., Jeong, J. W., and Lee, J. J., 2015, "Design Considerations for a Hyper-Redundant Pulleyless Rolling Joint With Elastic Fixtures," IEEE/ASME Trans. Mechatronics, **20**(6), pp. 2841–2852.
[43] Hirose, S., and Umetani, Y., 1978, "The Development of Soft Gripper for the Versatile Robot Hand," Mech. Mach. Theory, **13**(3), pp. 351–359.
[44] Catalano, M. G., Grioli, G., Farnioli, E., Serio, A., Piazza, C., and Bicchi, A., 2014, "Adaptive Synergies for the Design and Control of the Pisa/IIT SoftHand," Int. J. Rob. Res., **33**(5), pp. 768–782.
[45] Palli, G., 2006, *Model and Control of Tendon Actuated Robots*, Universita Di Bologna, Bologna, Italy.
[46] Cieslak, R., and Morecki, A., 1999, "Elephant Trunk Type Elastic Manipulator: A Tool for Bulk and Liquid Materials Transportation," Robotica, **17**(1), pp. 11–16.
[47] Wahl, A. M., 1944, *Mechanical Springs*, Penton Publishing Company, Cleveland, OH.
[48] Shames, I. H., 1998, *Engineering Mechanics: Statics*, Prentice Hall, Upper Saddle River, NJ.